Indian Ocean: Validation of the Miami Isopycnic Coordinate Ocean Model and ENSO events during 1958–1998

Vibeke E. Haugen, Ola M. Johannessen,[1] and Geir Evensen[2]

Nansen Environmental and Remote Sensing Center, Bergen, Norway

Received 3 March 2000; revised 19 June 2001; accepted 27 June 2001; published 25 May 2002.

[1] In the Indian Ocean, in situ data are sparse both in time and space. Therefore, numerical models are one of the major tools for further understanding of the ocean circulation. We have implemented, validated, and done a 40 year simulation experiment forced by synoptic atmospheric data by using the Miami Isopycnic Coordinate Ocean Model (MICOM) not previously used for the Indian Ocean. The simulation results compare well to available observations including an extensive altimeter data set from ERS and TOPEX/Poseidon. The model simulation discovered an anticyclonic gyre in the southern Bay of Bengal, confirmed by altimeter data and previously unknown. This gyre is clearly influenced by the strength of the Indian Monsoon Current. From the 40 year interannual investigation, abnormal cooling as high as 4°C was simulated off Indonesia, in the eastern part of the Indian Ocean, and warming in the west, off Somalia, during years which coincide with negative Southern Oscillation Index (SOI). These years also coincide with Pacific Ocean El Niño years, except for 1961. The cooling off Indonesia is normally followed by a warming the following year. We also observed a reduction in upwelling off the southwest coast of India, which is one of the major fishing areas along the continental shelf, which also coincide with El Niño–Southern Oscillation (ENSO) years. We conclude that El Niño events occur very clearly in the Indian Ocean. *INDEX TERMS:* 4215 Oceanography: General: Climate and interannual variability (3309); 4255 Oceanography: General: Numerical modeling; 4532 Oceanography: Physical: General circulation; 4556 Oceanography: Physical: Sea level variations; *KEYWORDS:* Indian Ocean, MICOM, circulation, sea level variations, El Niño

1. Introduction

[2] The circulation patterns in the Indian Ocean are forced by the southwest and northeast monsoonal winds. The southwest (SW) monsoon is normally observed from May to August/September, and the northeast (NE) monsoon is observed from October to January/February. However, the Indian Ocean is a region of great contrasts. In the Bay of Bengal (Figure 1), large rivers discharges and heavy rainfall result in low salinity, while the Arabian Sea has no major rivers draining into it but receives high-salinity water from the Red Sea and Persian Gulf.

[3] The ability to improve the understanding and predictability of the Indian Ocean circulation on timescales of annual to decadal in response to the monsoon system and feedback from ocean to atmosphere is of great importance to over a billion people living in the region. For example, in 1998–1999 the monsoon rains caused the water level to increase by >4 m in some places, and 20,000 hectares of land flooded. A million people lost their homes, and 300 died in India alone. Fishing was among the businesses which were struck the hardest.

[4] Modeling efforts in the Indian Ocean have not been as extensive as in other parts of the world's oceans. The Arabian Sea, particularly the Somali Current area, is the area in the Indian Ocean where most of the modeling effort has been focused. Some of the most recent studies include *Simmons et al.* [1988] who studied the upper layer circulation of the northwest Indian Ocean using a nonlinear reduced gravity model incorporating realistic boundary geometry and forced with 1985 observed winds. *Jensen* [1993] studied the equatorial variability using a wind driven layer model. *Anderson et al.* [1991] investigated the dynamics of the Somali Current system during the SW monsoon using a 16-level general circulation model, showing a number of model geometries and wind-forcing patterns. *Bruce et al.* [1994, 1998] studied the eddy formation in the eastern Arabian Sea during the NE monsoon, and *Shankar et al*. [1997] investigated the dynamics of the Lakshadweep High and Low, using a dynamic reduced gravity model for the north Indian Ocean. Modeling efforts in the Bay of Bengal have not been as extensive as in the Arabian Sea. Among some of the studies are those of *Potemra et al.* [1991], who used a multilayer numerical model driven by monthly winds, simulating the annual circulation in the upper Indian Ocean, and *Yu et al.* [1991] who used a simple reduced gravity model to study the remote forcing in the Bay of Bengal. *McCreary et al.* [1996] investigated the dynamics of the Eastern Indian Coastal Current (EICC) using a linear continuously stratified model, forced with Hellerman and Rosenstein winds [*Hellerman and Rosenstein*, 1983], and *Vinayachandran et al.* [1999a] studied the intrusion of the Indian Monsoon Current (IMC) using a model based on the Geophysical Fluid Dynamics Laboratory ocean model forced by Florida State University winds.

[5] In order to improve the modeling simulation we implemented and validated the isopycnic ocean model, the Miami Isopycnic Coordinate Ocean Model (MICOM), which is more complete and complex than those previously published in this area. The model was chosen because it has been validated and proven in other areas of the world's oceans with good results [*Bleck et al.*, 1992]. The overall objective of our investigations is to improve our understanding of the ocean circulation and variability in the Indian Ocean in response to the monsoon system and to study the interannual signals in the Indian Ocean over a 40 year period.

[1] Also at the Geophysical Institute, University of Bergen, Bergen, Norway.

[2] Also at the Mathematical Institute, University of Bergen, Bergen, Norway.

0148-0227/02/2000JC000330$09.00

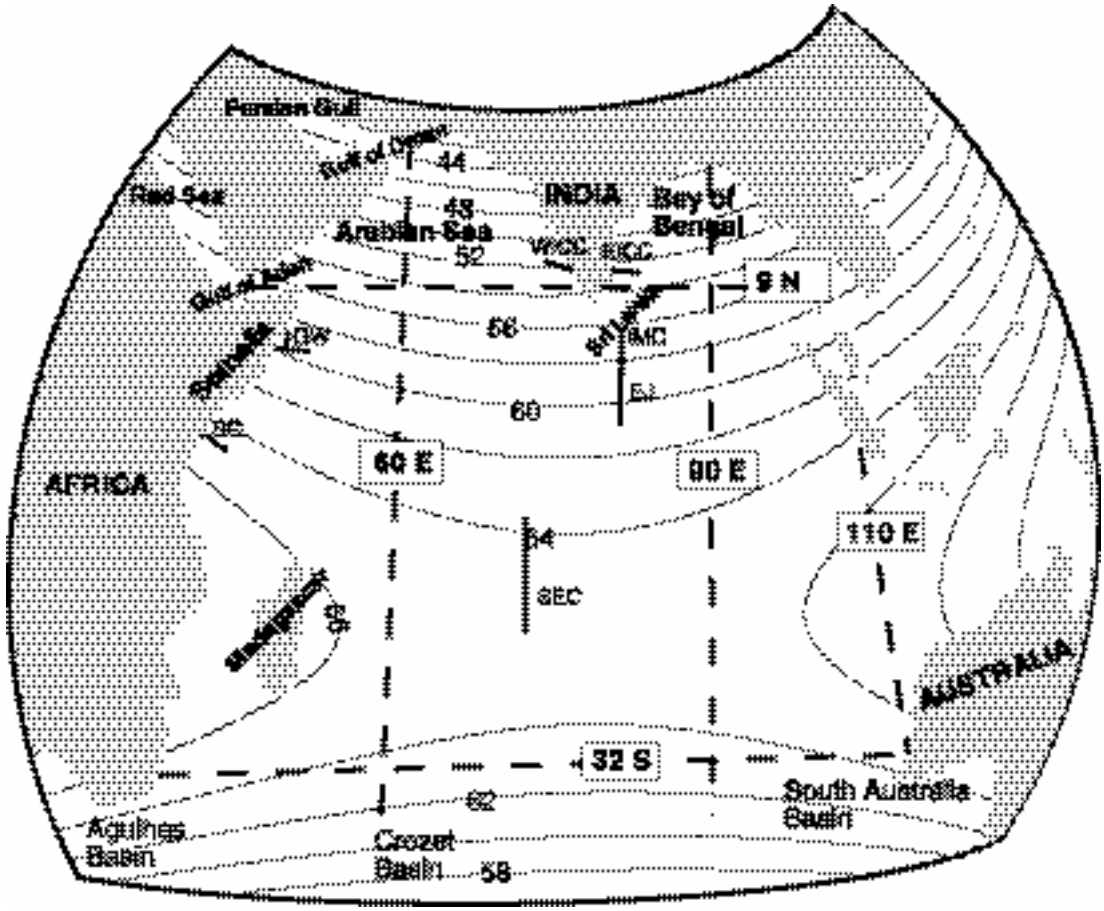

Figure 1. Model domain and horizontal resolution of the Indian Ocean. Labels show the resolution in kilometers. Dashed lines represents the meridional 60°E, 90°E, and 110°E and zonal 9°N and 32°S water mass sections plotted in Figures 11 and 12 and discussed in section 3.3. Thick lines are named and represent the transport sections plotted in Figure 9 and discussed in section 3.3.

[6] Section 2 describes the model setup and the altimeter data set used. Section 3 presents results from the validation of the model's simulated sea level anomalies (SLA) using altimeter data in addition to validation of the seasonal surface circulation, transport of currents, and the distribution of water masses using in situ data and previously published results from other models. Section 4 describes a 40 year numerical experiment using NECP forcing fields to study interannual variability in the Indian Ocean, including a 20 year simulation using European Centre of Medium-Range Weather Forecasting (ECMWF) data to study the effect on the ocean using different forcing fields. Finally, section 5 presents the conclusions from this experiment.

2. Model Setup

[7] The physical model used is based on MICOM, which is a dynamic-thermodynamic ocean general circulation model developed by *Bleck and Boudra* [1986], *Bleck et al.* [1989, 1992], and *Smith et al.* [1990]. The model solves the primitive equations, using a split-explicit numerical scheme [*Bleck and Smith*, 1990], and is in the horizontal discretized on a *C* grid. In the vertical, MICOM uses potential density as the coordinate. The present implementation of the model has 15 layers based on densities from the study area. The upper layer is a mixed layer which interacts with the atmospheric forcing through freshwater and heat fluxes and the transfer of wind stress through entrainment/detrainment processes when the mixed layer deepens/retreats. It is based on the bulk representation by *Gaspar et al.* [1990]. The different layers interact mainly through hydrostatic pressure forces, but there is also a vertical flux due to a specified diapycnal mixing.

[8] The model domain extends from 40°S to 26°N and 39° to 150°E (Figure 1). The Red Sea and Gulf of Oman are included; the western boundary coincides with the African coast, and the northern boundary is closed by land. An orthogonal curvilinear grid [*Bentsen et al.*, 1999] is used to enhance the resolution in the northern Indian Ocean, where the minimum grid distance is 42 km, sufficient to resolve the larger mesoscale features.

[9] The bathymetry used was interpolated to the model grid using an improved version of ETOPO5, named DS759.2 from the Terrain Base project conducted by the National Geophysical Data Center and World Data Center-A for Solid Earth Geophysics and for Marine Geology and Geophysics (NGDC/WDC-A). We have made a few changes to the depth in the Indonesian waters, as the Terrain Base described the ocean floor as one large, smooth bowl-shaped depression with maximum depth of 167 m in the Java Sea. In reality, the seafloor in this region has a maximum depth of ~50 m; no smoothing was applied.

[10] The model was initialized using Levitus data [*Levitus et al.*, 1994; *Levitus and Boyer*, 1994] and spun up over 10 years using climatological monthly means of atmospheric forcing data. The model was then run using a mixture of climatological (cloud cover from Comprehensive Ocean-Atmosphere Data Set (COADS)) and precipitation from *Legates and Willmott* [1990] and synoptic atmospheric fields (air temperature, sea level pressure, and relative humidity) from ECMWF. The wind stresses were calculated from

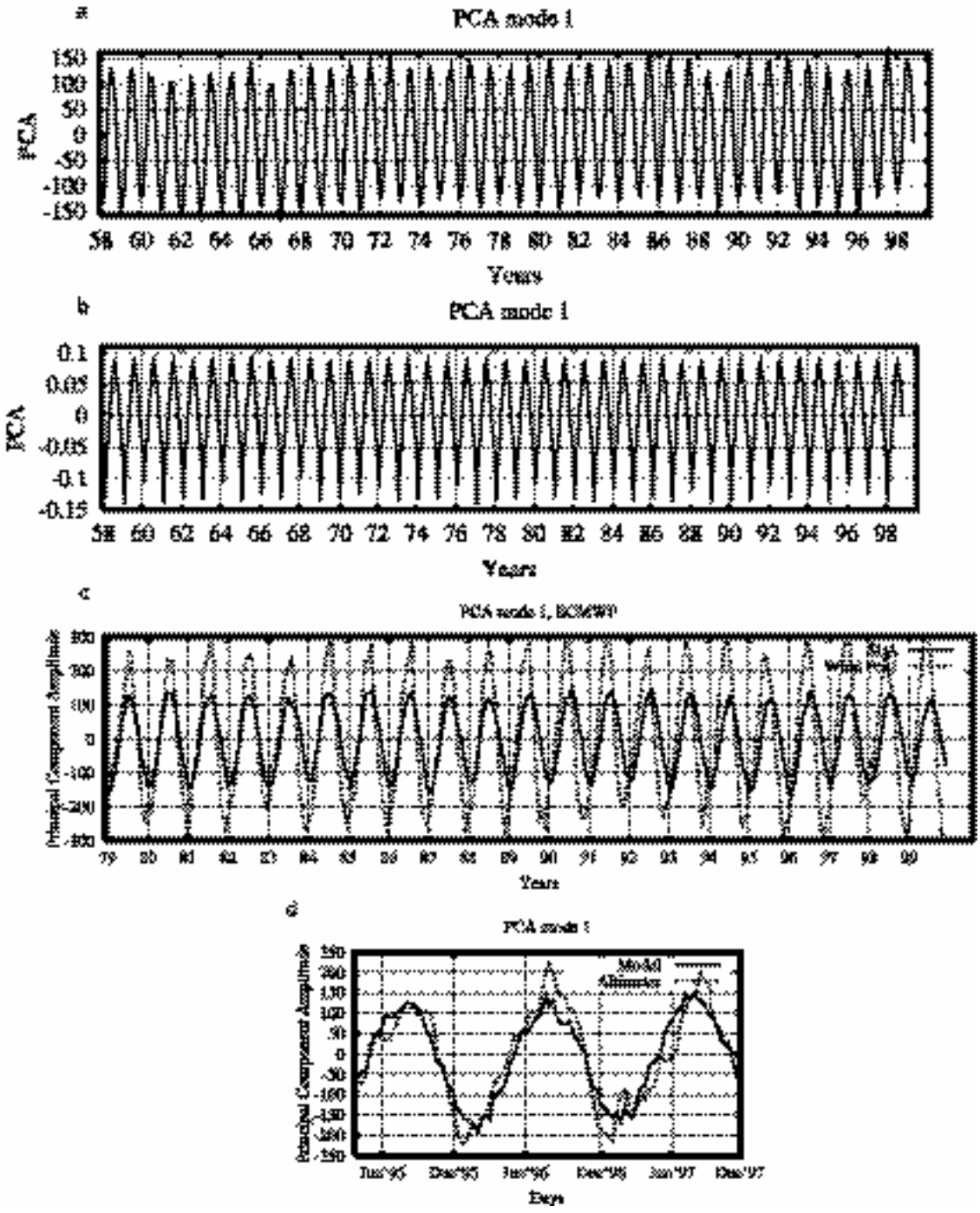

Figure 2. Principal component analysis (PCA) of (a) sea level anomolies (SLA), (b) sea surface temperature anomalies (SSTA), (c) zonal wind stress from ECMWF, and (d) simulated and observed (altimeter) SLA.

wind data which are available every 6 hours with a spatial resolution of $\sim 1^{\circ}$. Data have been bilinearly interpolated to the model grid and Hermitian interpolated in time. A weak surface relaxation with 50 days decorrelation time for salinity and temperature was used for all experiments. On the open boundaries we apply a relaxation of temperature and salinity to monthly averaged climatologies produced by a global version of MICOM (G. Evensen personal communication, 1999). The global model has a resolution of 1.5° and was also initialized using Levitus climatological data. The purpose of relaxing to the global model fields, rather than using Levitus data directly, is that we expect the global model fields to be smoother and in better dynamical balance than the original Levitus data.

[11] The mass flux is determined by evaporation minus precipitation and is implemented as a salt flux. The evaporation is computed on the basis of the latent heat flux and involves a transfer coefficient and the specific humidities of the surface water and air. The specific humidity of air is calculated from synoptic fields of relative humidity, sea level pressure, and air temperature. The freshwater flux from the Brahamaputra and Gagnes Rivers into the Bay of Bengal is included in the model, using monthly averages from the *United Nations Educational, Scientific, and*

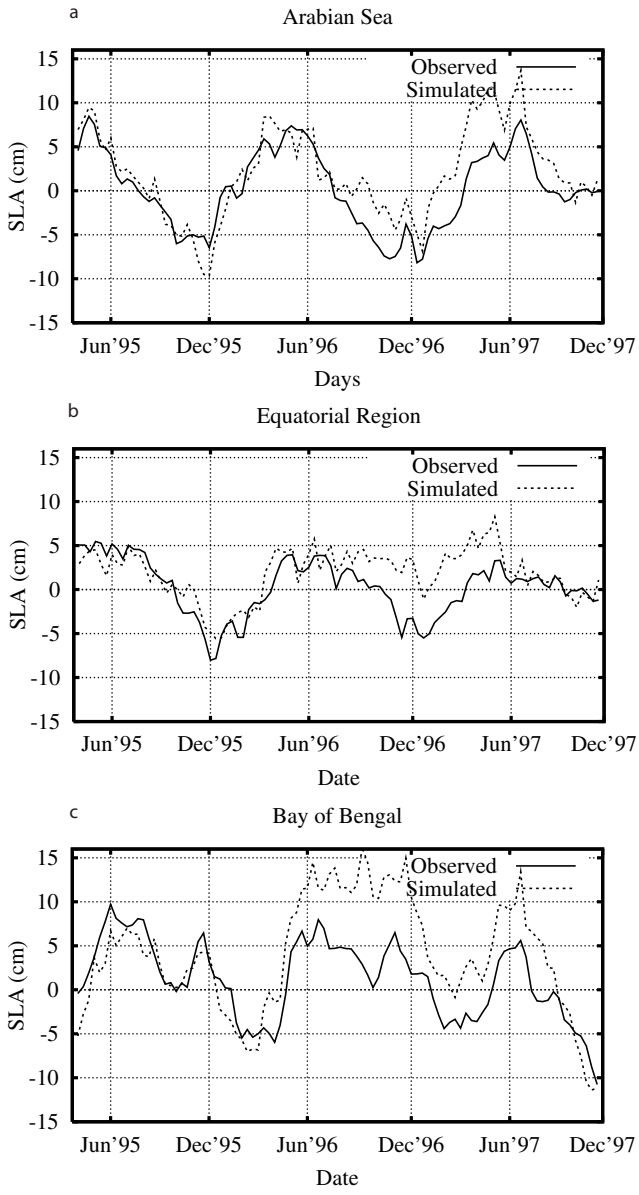

Figure 3. Basin-averaged observed and simulated SLA for (a) the Arabian Sea, (b) along equator, and (c) the Bay of Bengal.

Cultural Organization (*UNESCO*) [1993] database and *Perry et al.* [1996], and is used to update the mixed layer salinity. The freshwater flux is treated as a negative salinity flux. The energy flux through the ocean surface is computed based on fractional cloud cover, which influences the solar irradiance, the air and mixed layer temperatures, which determine the sensible heat flux, the evaporation, which gives the latent flux, and finally, the long wave radiation.

[12] The interdecadal study, 1958–1998, was run using synoptic National Centers for Environmental Prediction (NCEP) analysis data. To investigate the model's sensitivity to forcing, a 20 year integration, 1979–2000, using synoptic ECMWF forcing fields was also performed for comparison with the same period as NCEP forcing.

2.1. Altimeter Data Processing

[13] The combined ERS and TOPEX/Poseidon gridded Maps of Sea Level Anomaly (MSLA) altimeter data products (Collected Localisation Satellites (CLS) Space Oceanography Division, Ramonville, France, 1998) for the period 1995–1997, with a spatial resolution of 0.25° by 0.25° and a temporal resolution of 10 days, were used to validate the MICOM model, and interpolated to the model grid using a median filter. The MSLA products are generated from Archiving, Validation, and Interpretation of Satellite Oceanographic data (AVISO) Geophysical Data Records(GDR)-M products for TOPEX/Poseidon and from Centre ERS d'Archivage et de Traitement (CERSAT) ocean products (OPRs) for ERS altimeter data. These data have already been corrected for instrumental errors and environmental perturbations (wet and drytropospheric fitted to the more precise TOPEX/Poseidon data using a global minimalization of ERS and TOPEX/Poseidon dual-crossover differences [*Le Traon*, 1995; *Le Traon and Ogor*, 1998]). This provides ERS orbits with accuracy similar to TOPEX/Poseidon orbits of 2 cm RMS. The MSLA are obtained using an improved space-time objective analysis method which takes into account long-wavelength errors [*Le Traon et al.*, 1998].

3. Model Results and Validation

3.1. Sea Level

[14] The model's ability to reproduces the monsoon characteristics compared to altimeter data was studied for the period 1995–1997, when we have combined gridded ERS and TOPEX/Poseidon altimeter data. Principal Component Analysis (PCA) [*Preisendorfer*, 1988] was performed on SLA and sea surface temperature anomalies (SSTA) for both model integrations using different forcing fields (see section 4), on observed SLA from altimeter data, and on ECMWF zonal wind stress (Figure 2). The dominant mode (Figure 2d) which describes the annual signal accounts for 32.0 and 10.1% of the variance for the simulated and observed SLA, respectively. The difference between the two data sets is a reflection on the complexity of the underlying mesoscale processes, which span a wide range of temporal and spatial scales, and the fact that the model data are smoothed in a long-term simulation with a relatively coarse model resolution, while the observed SLA data are originally defined on a fine regular grid.

[15] Time series of observed and simulated SLA (long-term mean removed) (Figure 3) have been averaged over three areas for the same period to further study the model's ability in simulating SLA. In the Arabian Sea (5°–20°N, 40°–85°E), maximum amplitudes (8–15 cm) are reached during the SW monsoon for both data sets, with amplitudes a few centimeters higher for the simulated data (Figure 3a). In the Bay of Bengal (5°–20°N, 85°–100°E) maximum amplitudes (6–15 cm) are reached during both monsoon periods (Figure 3c). In 1996 the difference in amplitude for simulated and observed SLA is much higher than for the rest of the study period, which might be due to model deficiencies, e.g., inaccuracy in the forcing fields. In addition, the Bay of Bengal is bounded by land, so the likely reasons for the difference might be the altimeter errors near shore. The observed annual periods were also shown in the PCA and confirm the model's ability to reproduce the monsoon characteristics. The model performs best in simulating the SLA in the equatorial area (5°S–5°N, 40°–100°E; Figure 3b), probably because this is a region of lower mesoscale variability than the Arabian Sea and Bay of Bengal and because it is a region not bounded by land. Also, here we observe an annual signal, with peaks during the SW monsoon.

[16] Hovmöller diagrams (longitude versus time plots) are shown for 15°N, 10°N and 10°S, and 5°N and 5°S (Figure 4). Areas of simulated positive and negative SLA compare well with altimeter SLA, although model SLA amplitudes are stronger. These anomalies are intepreted to be westward propagating upwelling and downwelling Rossby waves, which will be further discussed in section 4, together with a discussion on the propagation speed. The correlation coefficient computed for the selected latitudes between the observed and simulated SLA is good. With a decrease in model

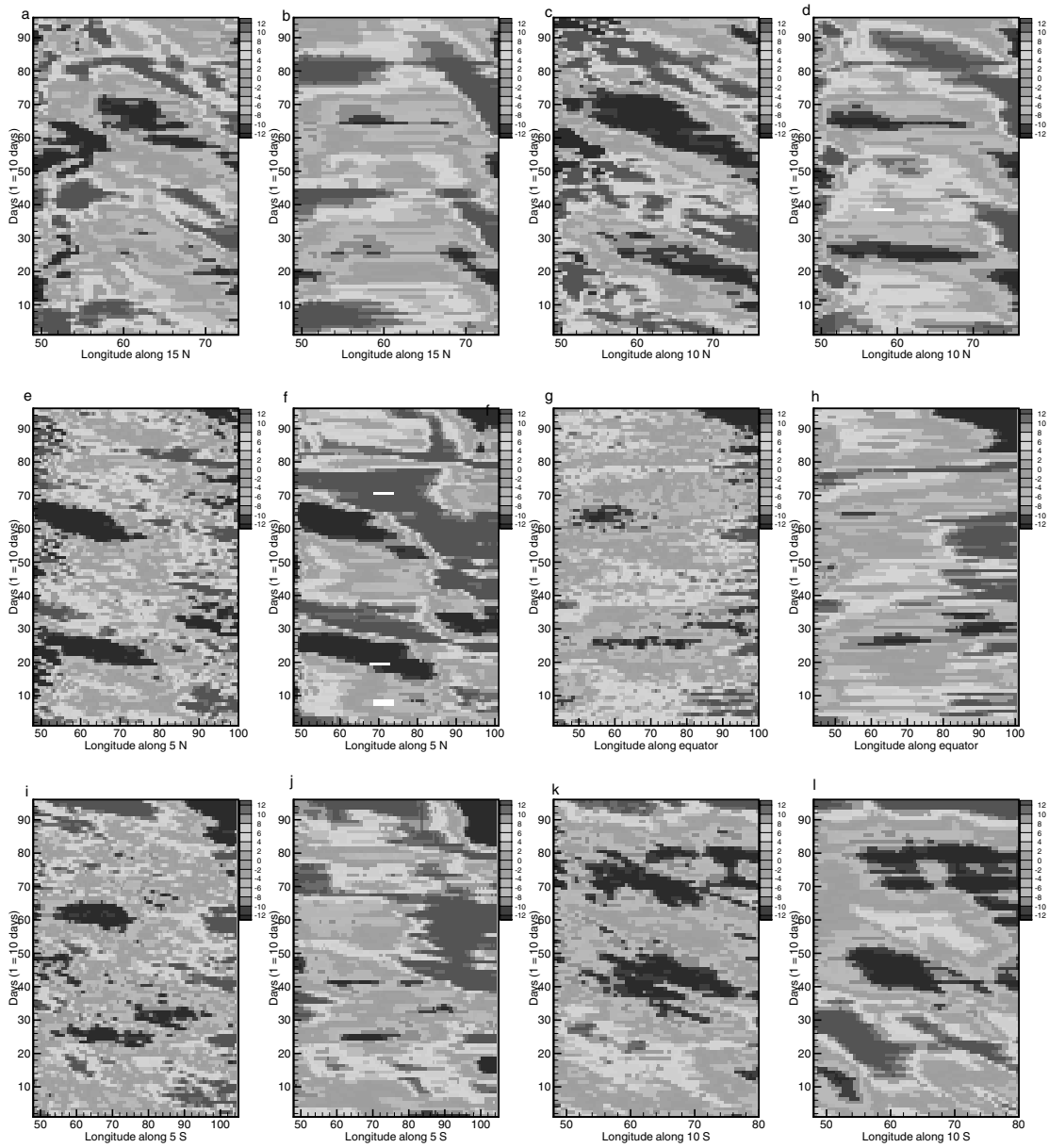

Figure 4. Hovmöller plots from observed (left plot in each pair) and simulated SLA (right plot in each pair) every 5° latitude between 15°N and 10°S from 1995 to 1997 (y axis: 1 = 10 days). See color version of this figure at back of this issue.

resolution the correlation also decreases, which is especially seen for latitudes south of 10°S, where the correlation is only 0.5 on average, compared to values above 0.6 north of equator.

[17] Correlations computed for the period 1995–1997 (Figure 5a) show best results in low-variability areas. High correlation, between 0.75 and 1.0, is observed along the equator and the southeastern and northern Indian Ocean but less in the interior of the Bay of Bengal. The southwestern area, which is a high-variability area, also shows low correlation. We also observe that there is somewhat less correlation in areas near the coast owing to altimeter errors near shore. *Yang et al.* [1998] concluded that the reasons for poor model-data agreement were the use of a model without thermodynamics and Indonesian Through flow. In the present model this is included, but areas of low correlation are still the same. However, we suggest that the lack of correlation indicates that the onset/decay of the whirls and currents are different in the two data sets and that a higher-resolution model is needed in order to simulate the observed anomalies.

3.2. Indian Ocean Surface Circulation

[18] In this part of the validation we have focused on the circulation influenced by the monsoon seasons and therefore concentrate our analysis in the area north of 10°S, which we have divided into three areas, the equatorial region, the Arabian Sea, and the Bay of Bengal. The model surface circulation is seen in Figure 6, where the thick lines represent a summary of the surface circulation as reported by previous investigators. A summary of the comparison of speeds from simulated currents with available model and in situ observations discussed below is presented in Table 1.

3.2.1. Between 10° and 20°S. [19] In the southern part of the tropical Indian Ocean the surface currents are persistent in the course of the year. The Southern Equatorial Current (SEC) is the

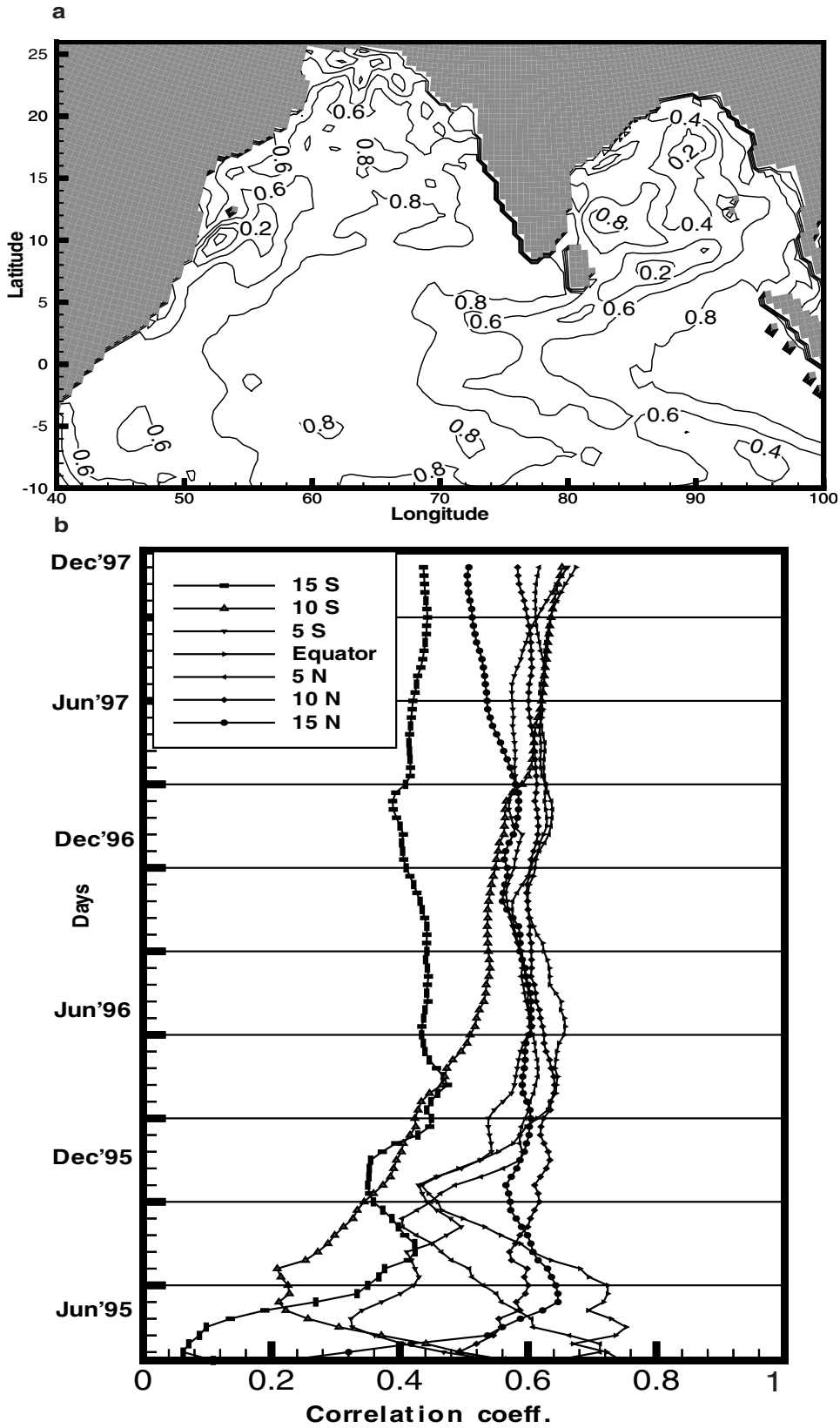

Figure 5. Correlation coefficient computed for observed and simulated SLA (a) in time for the northern Indian Ocean and (b) in space for selected latitudes.

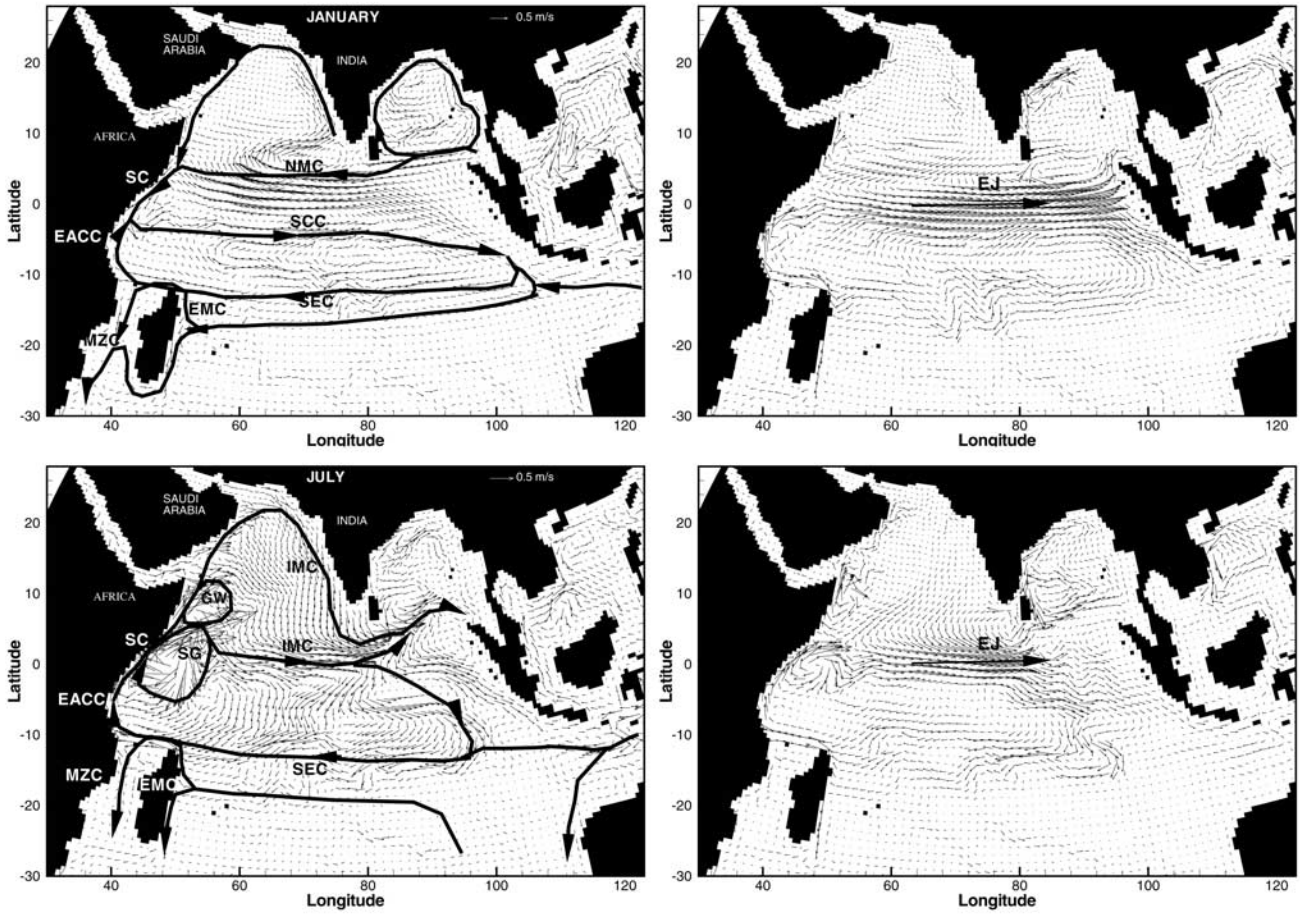

Figure 6. Monthly averaged surface circulation in the Indian Ocean for January, April, July, and October 1996 from the model. Every second vector is shown. Thick lines represent the circulation as observed from previous investigations. SEC, Southern Equatorial Current; MZC; Mozambique Current; EMC, Eastern Madagascar Current; SCC, Southern Counter Current; EACC, East African Coastal Current; SC, Somali Current; IMC, Indian Monsoon Current; NMC, Northeast Monsoon Current; SG, Southern Gyre; GW, Great Whirl.

strongest current of the southern tropical Indian Ocean, located south of 10°S [*Hastenrath and Greischar*, 1991] and is simulated by the model between 10° and 20°S throughout the year (Figure 6). Peak speeds of 40 cm/s are observed from our simulations during the Southern Hemisphere winter, which is in agreement with ship drift climatology current measurements reported by *Rao et al.* [1989] and reported speeds from buoys [*Molinari et al.*, 1990]). During the SW monsoon the SEC intensifies on the African side and separates into southward and northward branches. The latter feeds the northward flowing East African Counter current (EACC), which is important to the Somali Current (SC), and forms a basin-wide gyre with the Southern Counter current (SCC). This is well simulated by our model between the equator and 8°S and dominates the southern part of the Indian Ocean.

3.2.2. Equatorial region. [20] During winter (Figure 6a) the westward flowing Northeast Monsoon Current (NMC) is simulated, extending between 8°N and the equator. In January our simulations show speeds which exceed 100 cm/s, which compare well with 90 cm/s as reported by *Schott et al.* [1994]. With the onset of the SW monsoon (Figure 6c) the NMC reverses direction and joins the SCC to form the Indian Monsoon Current (IMC), which appears between the equator and 9°N. The IMC is also fed by the Somali Current. Our simulations show speeds of 40 cm/s for the IMC, which is in good agreement with *Vinayachandran et al.*'s [1999b] speeds of 40 cm/s from expendable bathythermograph (XBT) sections but greater than their results of 25 cm/s calculated from altimeter data and a model based on the Geophysical Fluid Dynamics Laboratory ocean model. In November, after the transition to the NE monsoon, the NMC returns to its westward flow.

[21] During the transition periods, April–May and October–November (Figures 6b and 6d), eastward winds over the equator drive the Wyrtki equatorial jet eastward across the entire Indian Ocean [*Wyrtki*, 1973]. It appears in April and May and then again in October. The jet is strongest between 60° and 90°E, where surface speeds often exceed 64 cm/s; even 215 cm/s speeds have been reported by *Wyrtki* [1973]. *Cutler and Swallow* [1984] reported speeds of 80–100 cm/s from their ship drift climatology data and *Reverdin* [1987] reported speeds of 40–50 cm/s from a wind-forced linear model. Our simulations show monthly averaged speeds up to 130 cm/s during April and as high as 160 cm/s during the end of April, between 70° and 90°E. In October/November, speeds up to 100 cm/s have been simulated, in good agreement to the above investigations.

3.2.3. Arabian Sea. [22] During April/May the strong northward coastal current, the SC, fed by the SEC/EACC, appears (Figure 6). The model simulates the SC with a maximum weekly averaged speed during the beginning of July

Table 1. Summary of the Comparison of Characteristic Speeds From the Simulated Currents With Available Model and In Situ Observations[a]

Current	Observation/ Model[b]	Observation Time	Observation Speed	MM Time	MM Speed
SEC	ship drift (1)	winter	40 cm/s	winter	40 cm/s
SEC	buoys (2)	winter	+30 cm/s		
IMC	XBT (3)	SW	40 cm/s	SW	40 cm/s
IMC	altimeter (3)	SW	25 cm/s		
IMC	model (3)	SW	25 cm/s		
NMC	ship drift (4)	Dec.–Jan.	90 cm/s	January	100 cm/s
EJ	in situ (5)	transition	64–215 cm/s	October	80–100 cm/s
EJ	ship drift (7)	transition	80–100 cm/s	April	130–160 cm/s
EJ	model (6)	transition	40–50 cm/s		
SC	in situ (8)	SW	3 m/s	SW	2 m/s
SC	model (9)	SW	+1 m/s		
SC	model (10)	SW	1.4 m/s		
GW	ADCP (11)	August	2.2 m/s	SW	1.0–1.7 m/s
EICC	geostrophic calculation (12)	Dec.–April	66 cm/s	NE	60–70 m/s
EICC	buoys (13)	Feb.–March	62 cm/s	Feb.–March	60–70 m/s
EICC	buoys (1000 m) (13)	Feb.–March	17 cm/s	Feb.–March	14–18 m/s

[a] MM, MICOM model; Southern Equatorial Current, IMC, Indian Monsoon Current; NMC, Northeast Monsoon Current; EJ, Equatorial Jet; SC, Somali Current; GW, Great Whirl; EEIC, Eastern Indian Coastal Current; XBT, expendable bathythermograph; ADCP, acoustic Doppler current profiler.

[b] Numbers in parentheses refer to the following references: 1, *Rao et al.* [1989]; 2, *Molinari et al.* [1990]; 3, *Vinayachandran et al.* [1999b]; 4, *Schott et al.* [1994]; 5, *Wyrtki* [1973]; 6, *Reverdin* [1987]; 7, *Cutler and Swallow* [1984]; 8, *Swallow et al.* [1983]; 9, *Anderson* [1991]; 10, *Hurlburt and Thompson* [1976]; 11, *Fisher et al.* [1996]; 12, *Shetye et al.* [1996]; 13, *Varkey et al.* [1996].

of 2 m/s, which is lower than *Swallow et al.*'s [1983] measured speeds from in situ data of 3 m/s near the Somali coast. *Hurlburt and Thompson* [1976] reported that speeds up to 3 m/s have been observed, but their 2-layer nonlinear numerical model results showed maximum speeds of only 1.4 m/s during the SW monsoon. Also, *Anderson et al.*'s [1991] model showed speeds in slight excess of 1 m/s for the SC. Two cyclonic gyres were simulated well in June/July with the onset of the strong wind stress curl, the Great Whirl (GW), centered at ~8°N and with a radius of ~350 km, and the Southern Gyre (SG), located in the area 0°–5°N, 53°E. Slightly northeast of the GW, the Socotra Gyre, with a diameter of ~200 km, is simulated only during the peak of the SW monsoon, during July–August. The model's resolution is obviously too coarse to simulate this and other smaller mesoscale features, <200 km in diameter [*Simmons et al.*, 1988]. During the onset of the NE monsoon the SC reverses direction and flows southward along the coast to ~2°–3°S, where it merges with the northward flowing EACC, and then both turn offshore into the SCC [*Schott et al.*, 1994].

[23] The monsoon circulation was confined to the upper 300 m depth with intense surface currents up to 2.2 m/s for the GW measured from shipboard acoustic Doppler current profilers (ADCPs) during August [*Fischer et al.*, 1996], which is higher than our simulated speeds of 1.0–1.7 m/s during August.

[24] Along the western coast of India the southward flowing coastal current, Western Indian Coastal Current (WICC), has been simulated from April to September. In October it reverses direction and flows northward until March, as also observed by *Johannessen et al.* [1981] and *Shetye et al.* [1991]. An undercurrent of opposite direction is also simulated during the two monsoon periods in agreement with *Antony* [1990] and *Shetye et al.* [1990].

[25] The model also simulates the large anticyclonic eddy, Laccadive High (LH), with a diameter of 500–800 km [*Bruce et al.*, 1994] (Figures 7a and 7b), which is positioned off the southwestern India (centered near 10°N, 70°E during the NE monsoon) in January. In February–March it is simulated as it stretches westward in accordance with *Shankar and Shetye*'s [1997] observations. The cyclonic eddy, Laccadive Low, centered near 7°N, 76°E from hydrographic and altimeter data, has been observed from July to October by *Shankar and Shetye* [1997] but was only simulated during October in our simulations (not shown), possibly because of the coarse model resolution.

3.2.4. Bay of Bengal. [26] The Bay of Bengal is a semi enclosed tropical basin under the influence of monsoonal wind and freshwater inflow, causing a strong stratified surface layer. The currents in the Bay of Bengal also reverse their direction semiannually, in response to the monsoon system. Three major gyres which have previously been reported in the Bay of Bengal have been simulated (Figure 7), and these will be described first. These are the northwestern gyre (G1) between the coastline, 13°N and 89°E, which is anticyclonic during winter and cyclonic in summer; an anticyclonic southern gyre (G2) in the area south of 13°N; and a double gyre (G3) in the Andaman Sea with anticyclonic and cyclonic flows for both seasons [*Varkey et al.*, 1996]. In addition, our observations include a new cyclonic gyre in the southern Bay of Bengal not previously reported, hereafter named G4, which will be described last.

[27] The model simulates (Figure 7) the seasonally reversing coastal current EICC in the western part of the basin. The EICC intensifies in our simulation in February–March, in agreement with *Shetye et al.*'s [1993] results, and flows northward until the SW monsoon weakens. It then begins to flow southward along the Indian and Sri Lankan coasts from October to January when it decays and then again begins to flow northward in February. The EICC forms the western branch of the anticyclonic G1 gyre during winter (December–April), which is driven by the NE monsoon winds. From simulations we observe the western branch with surface speeds of 60–70 cm/s during February–March, which is in agreement with *Varkey et al.*'s [1996] speeds of 62 cm/s from buoys and *Shetye et al.*'s [1996] geostrophic calculations of 66 cm/s. At depths of 600 m the speeds have been reduced to 15–25 cm/s, which is slightly greater than the speeds in excess of 10 cm/s reported by *Shetye et al.* [1996]. Deeper, between 800 and 1000 m, our simulations show speeds of 14–18 cm/s, which is in agreement with *Varkey et al.*'s [1996] speeds of 17 cm/s at 1000 m. In May, when G1 reverses direction, the flow is northward along both coasts of the bay, and G1 is formed into two cells of opposite direction (Figure 7c). The southern cell is fed by the northward flowing EICC, and the cyclonic northern cell is fed by the EICC in the eastern part of the basin. By June, G1 has become cyclonic and lasts until September. In May the EICC starts reversing. Below

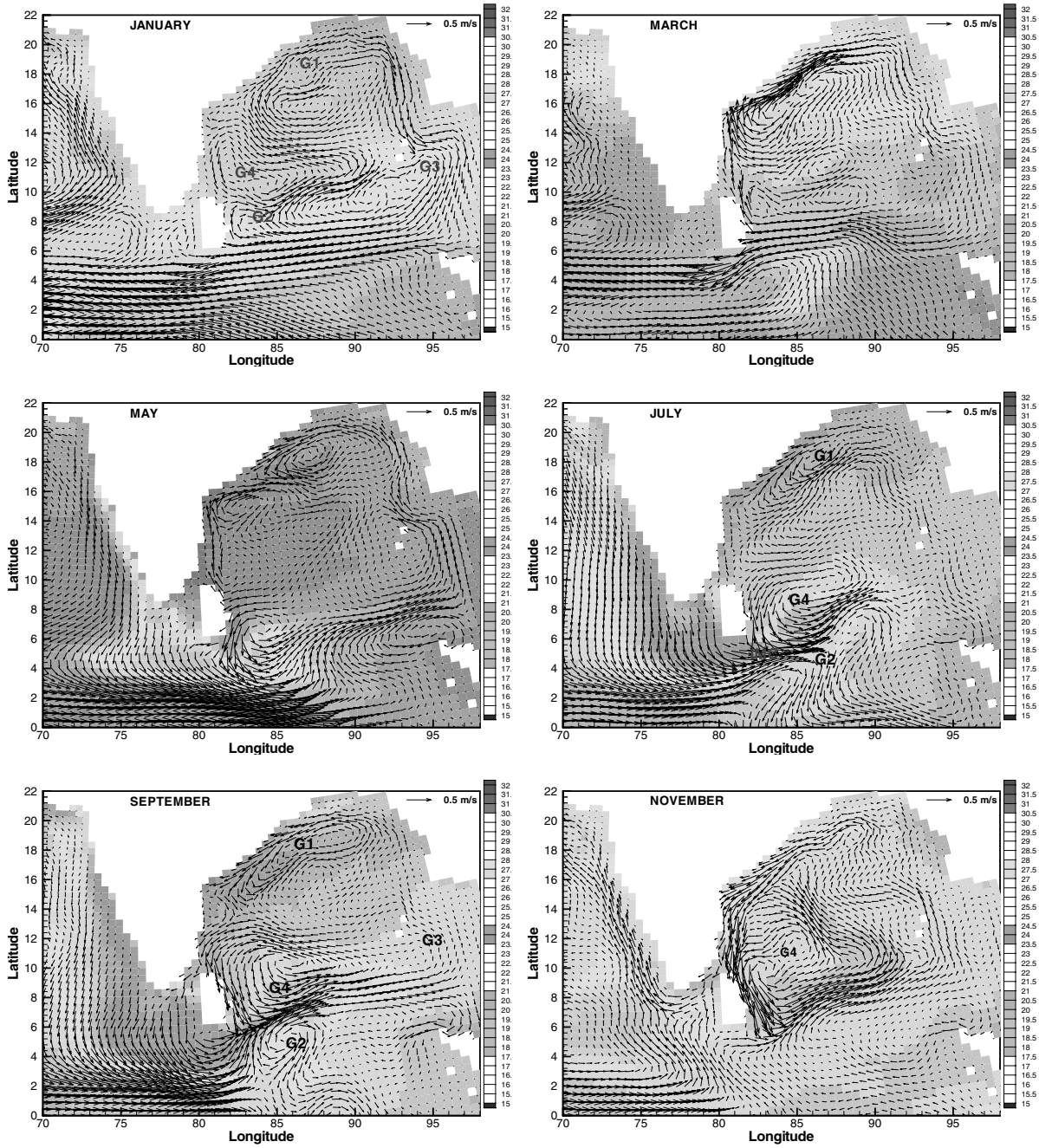

Figure 7. Surface circulation in the Bay of Bengal from the model showing temperature and current velocities for every second month from January to November 1996. G1 to G4 represent the eddies which are discussed in section 4, and IMC is the Indian Monsoon Current. See color version of this figure at back of this issue.

16°N it flows southward, and by July it has extended along the whole coast of India and flows southward until December. Below the EICC we simulated an undercurrent of opposite direction in agreement with *Shetye et al.*'s [1993] observations from oceanographic data.

[28] In February/March the NMC develops into two branches at the eastern coast of Sri Lanka (Figure 7), where the northern branch develops into an anticyclonic cell, and the southern branch develops into a cyclonic gyre. This two-gyre system has also been reported by *Shetye et al.* [1993] and *Potemra et al.* [1991] during the transition period.

[29] The anticyclonic gyre G2 is simulated during January–March and is formed by a branch of the NMC which turns northward when it reaches the eastern coast of Sri Lanka. It propagates eastward in July with speeds as high as 50–60 cm/s. In June the eastward flowing IMC has been developed and forms two counter rotating cells east of Sri Lanka. The southern cell is the anticyclonic G2, which in June is split into two anticyclonic cells which are seen to merge in July. During summer the G2 gyre forms the southern boundary of this area and is simulated during both monsoon periods, although in summer it is slightly farther south than what was reported by *Varkey et al.* [1996].

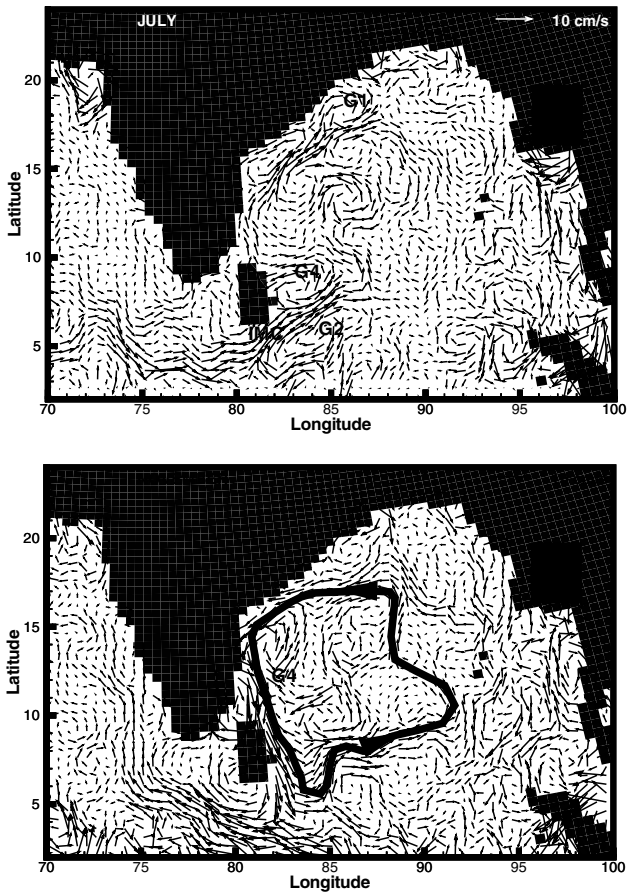

Figure 8. Geostrophic currents calculated from monthly mean observed anomalies for July and November 1996 from the altimeter data.

[30] Between July and September the cyclonic G3 in the eastern part of the bay was simulated, in agreement with *Varkey et al.*'s [1996] results. In June and between November and January we simulated it as an anticyclonic gyre.

[31] The model simulates the gyres G1, G2, and G3 well, and we therefore have confidence in the simulation of the not previously reported G4 cyclonic gyre simulated north of G2. This gyre intensifies with the increase of the SW monsoon and reaches a maximum in extent after the SW monsoon, during September–November. In October it is located between 5° and 14°N and between the coast of India and 91°E, before it starts to decay in December. The circulation in the southern part of the Bay is strongly influenced by the wind, and years identified as El Niño years in the Pacific Ocean reverse the westerlies at equator and weakens the IMC, which again affect the gyre. In October 1997 the gyre is simulated with a diameter of 400 km and a displacement farther north, while during non–El Niño years the diameter in the zonal direction is of the order 800–1000 km. In October–November during non–El Niño years the southern boundary of the gyre flows eastward with speeds of 50–55 cm/s. At 92°E it flows northward with a speed of 25–30 cm/s. Between 10° and 12°N the gyre stretches as far west as 85°E, with speeds between 20 and 30 cm/s, before it again turns eastward. Between 13° and 15°N the gyre flows westward with a speed of 40 cm/s and grows until January/February, when it starts to decay. These velocities agree well with hydrographic data from *Babu et al.* [2000]. Our calculations of geostrophic currents from SLA, averaged over a month, confirmed the location of this eddy (Figure 8) which then is a new confirmed feature of the Bay of Bengal circulation.

3.3. Transport

[32] Volume transport has been computed for selected sections (see Figure 1, thick lines), passing through the major currents simulated by the model, and validated with in situ or model data whenever available. Table 2 provides a summary of the following discussion. Total transports are calculated as the

Table 2. Summary of Comparison of Volume Transport Calculated Using the MICOM Model With Other Available Data[a]

Section	Observation/ Model[b]	Observation Time	Observation, Sv	MM Time	MM, Sv
NMC	moorings (1)	Jan.–Feb. 1991	12.8	Jan.–Feb.	10 Sv
NMC	moorings (1)	Jan.–Feb. 1992	10.4	Jan.	15
NMC	model (2)	Jan.	15.4		
IMC	moorings (1)	June 1991–1992	15	June 1992	10.5
IMC	moorings (3)	Aug. 1993	9.7	Aug. 1993	7–12.4
IMC	XBT (4)	May–Sept.	10		
IMC	XBT (4)	July	12		
SEC	model (5)	annual	24.3	annual	37
SEC	in situ (6)	NE	33–39	Jan.	29
EJ	geostrophic calculation (7)	April/May	22.5	April/May	26
EJ	Geostrophic calculation (7)	Oct./Nov.	14	Oct./Nov.	13–30 = 20
SC	model (5)	Aug.	20.5	July	18
SC	model (5)	July	10		
SC	moorings (7)	SW (500 m)	21	July (500 m)	31
SC	moorings (7)	SW (100 m)	11.4		
SC	ship observation (8)	July (200 m)	40		
GW E-W	XBT (9)	Oct. 1984	33.5 (250 m)	SW (500 m)	24
GW E-W	XBT (9)	Oct. 1984	31.6 (250 m)		
GW N-S	ADCP (9)	SW	58	SW	60
EICC	geostrophic calculation (10)	NE	10	NE	4–5
EICC	model (2)	NE	5	NE	4–5
EICC	hydrographic (11)	NE	7.7	NE	8–9

[a] See Table 1 for abbreviations.

[b] Numbers in parentheses refer to the following references: 1, *Schott et al.* [1994]; 2, *Bruce et al.* [1998]; 3, *Reppin et al.* [1999]; 4, *Vinayachandran et al.* [1999b]; 5, *Woodberry et al.* [1989]; 6, *Wyrtki* [1971]; 7, *Wyrtki* [1973]; 8, *Bruce* [1983]; 9, *Fischer et al.* [1996]; 10, *Shankar et al.* [1996]; 11, *Shetye et al.* [1996].

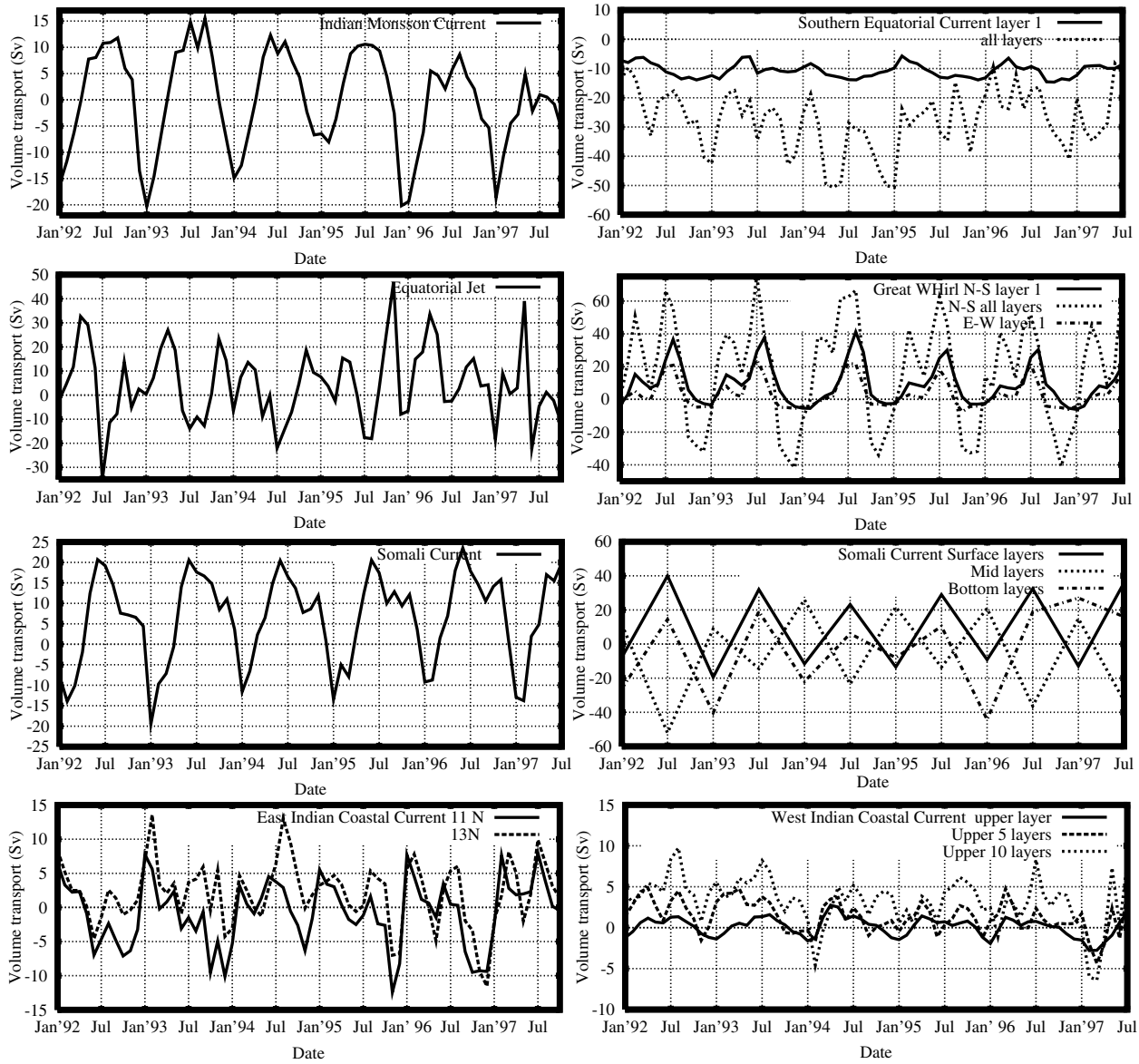

Figure 9. Timeseries of volume transports calculated for sections through the Indian Monsoon Current, Southern Equatorial Current, Equatorial Jet, Great Whirl, Somali Current, Somali Current in different layers at the peak of the monsoon periods, East Indian Coastal Current, and West Indian Coastal Current.

difference between the transport in and opposite to the reference direction, and positive Sv represents either eastward or northward transport.

3.3.1. Indian Monsoon Current and Northeast Monsoon Current. [33] The seasonal variability of the IMC and NMC is clearly seen in Figure 9, which shows the volume transport calculated for the section 2°–6°N at 80°E for the upper 300 m for the period 1992–1997. The IMC indicates an average eastward transport of 10 Sv during the SW monsoon (June–August). The westward transport of the NMC during the NE monsoon is slightly higher, with an average of 15 Sv in January. The transport of the IMC is primarily confined to the upper 300 m, and it is confined to the upper 500 m for the NMC. Averaging the volume transport for the NMC over January–February gives 10 Sv, ranging between 7.0 and 14.4 Sv, within the range of *Schott et al.*'s [1994] results, who reported a westward flowing NMC of 12.8 Sv in January–February 1991 and 10.4 Sv in 1992. From a reduced gravity model with three active layers forced with wind stress, *Bruce et al.* [1998] reported the NMC to have a volume transport in January of 15 Sv in the upper 300 m, in good agreement with our results. The IMC was simulated with a transport of 9.7 Sv during the beginning of August 1993 by *Reppin et al.* [1999], which also is in agreement with our results. *Vinayachandran et al.* [1999a, 1999b] reported a mean transport during the SW monsoon of 10 Sv from XBT sections, with a peak in July of 12 Sv, which is consistent with our simulations of transports between 7.0 and 12.4 Sv for August.

[34] Current moorings show eastward transports of 8 Sv north of 3.45°N at 80.3°E, south of Sri Lanka, for the IMC during June 1991–1992 [*Schott et al.*, 1994]. Their analysis was extended south to 2°N, and an increase from 8 Sv to ~15.4 Sv was observed. This was also the case in our simulations during the SW monsoon in 1992 and 1994, but for the rest of the study period, not much effect was seen. In June 1992 we observed an increase from 5–6 to 10.5 Sv.

3.3.2. Southern Equatorial Current. [35] The SEC flows westward with an annual model mean transport of 37 Sv integrated over all layers for the 5 years plotted in Figure 9, with ~10 Sv

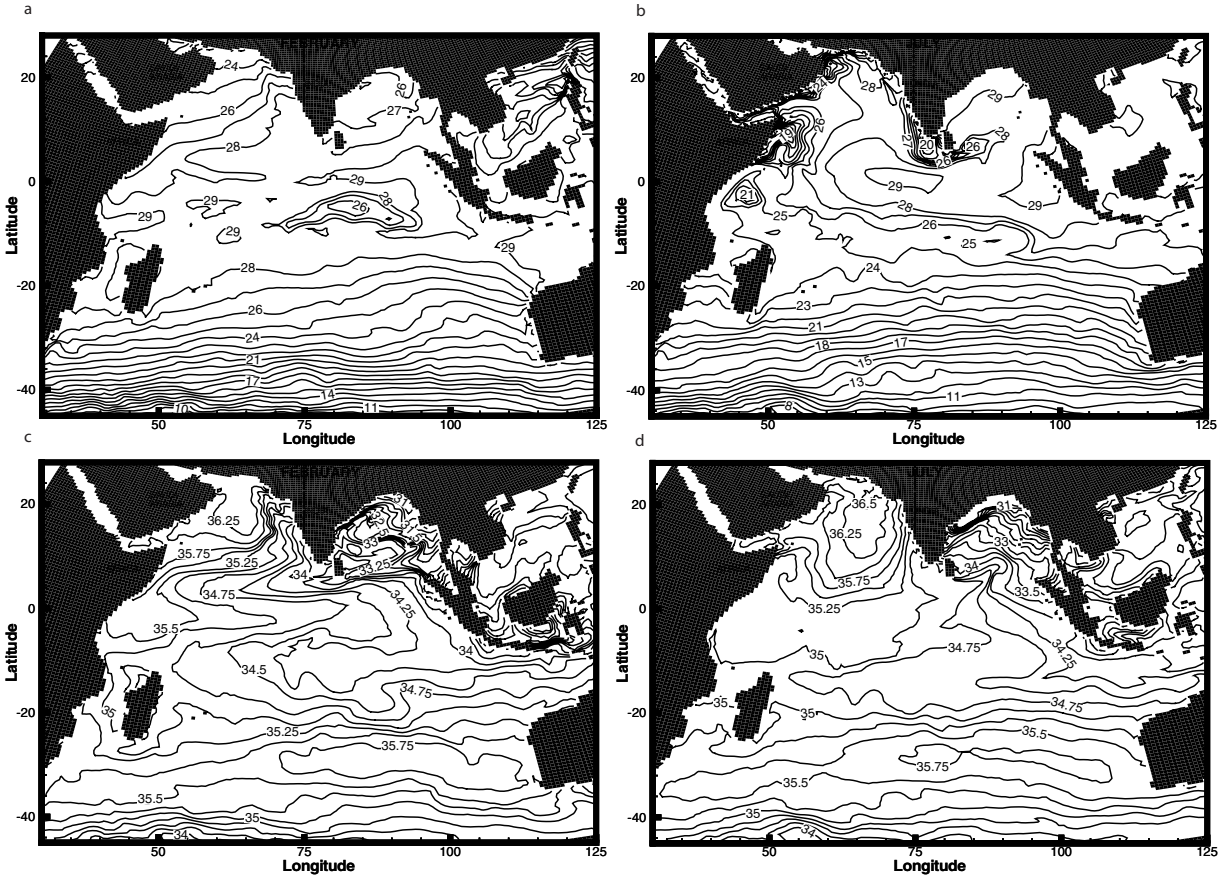

Figure 10. (a and b) Monthly averaged surface temperature and (c and d) salinity during February (Figures 10a and 10c) and July 1996 (Figures 10b and 10d) from the model. Salinity has a contour interval of 0.25 psu, and temperature has a contour interval of 1°.

confined to the surface layer (upper 100 m). The transport is normally strongest during the monsoon periods, with a mean in January of 29 Sv and in July of 24 Sv. Maximum transport of 50 Sv was observed in 1994 during May and November–December. *Woodberry et al.* [1989] reported an annual mean transport of 24.3 Sv from their model, driven by climatological monthly mean winds, which is lower than what our simulations show. The SEC has also been observed with transports between 33 and 39 Sv during the NE monsoon [*Wyrtki*, 1971], which is more within the range of our simulations.

3.3.3. Equatorial Jet. [36] The equatorial section, between 2°S and 2°N at 80°E (Figure 9), shows a volume transport for the EJ of 22 Sv in April–May, ranging between 12 and 32 Sv in the upper 100–200 m, and in October–November of 23 Sv, ranging between 12 and 47 Sv, averaged over a 5 year period. The mean is greater than *Wyrtki*'s [1973] estimates of 22.5 Sv in April–May and 14 Sv in October–November. If we exclude the maximum peak in October 1995 of 47 Sv, we have an average of 17 Sv over 4 years instead, which is more in the range of *Wyrtki* [1973].

3.3.4. Somali Current. [37] The seasonal reversing Somali Current (Figure 9) flows northward during the SW monsoon with a monthly mean volume transport during July of 18 Sv in the upper 100 m and 31 Sv in the upper 500 m. Previous results range between 10 Sv from *Woodberry et al.* [1989] to 40 Sv in the upper 200 m from *Bruce* [1983]. *Schott et al.* [1990] reported a summer mean of 21 Sv for the upper 500 m from current moorings, and *Woodberry et al.* [1989] reported a peak transport in August of 20.5 Sv from their model simulations.

[38] During the NE monsoon an averaged southward transport of 12.4 Sv is observed in January in the surface, and below we observe a northward undercurrent with an averaged transport of 20 Sv. Below this, in the deep layers, the flow reverses again, and we observe a strong southward flow with a transport between 10 and 20 Sv, less than the Somali Current (illustrated in Figure 9).

3.3.5. Great Whirl. [39] The "interior" volume transport for the GW was calculated at two sections, one capturing the north-south flow at 8°N between 50° and 55°E and one capturing the east-west flow at 50°E between 8° and 10°N (Figure 9). The northward flow has an average volume transport of 60 Sv over the whole water column, and almost 40 Sv is confined in the upper 100 m. This compares well with results from *Fischer et al.*'s [1996] study using a conductivity-temperature-depth/acoustic Doppler current profiler, which estimated a transport of 58 Sv for the GW. The eastward flow has an average volume transport of 24 Sv during the SW monsoon in the upper 500 m, where 20 Sv is confined to the surface layer. Below a weak westward flow is simulated. Estimates derived from shipboard acoustic Doppler radar current profilers and using geostrophy relative to 400 dbar from XBT lines estimated the GW transport in 1984 in the upper 250 m to be 33.5 Sv westward between 6° and 8.5°N and 31.6 Sv eastward between 8.5° and 11.5°N [*Schott and Fieux*, 1985].

3.3.6. Eastern Indian Coastal Current. [40] The seasonal reversal of the EICC can be seen from Figure 9 as southward during the SW monsoon and northward during the NE monsoon. The northward volume transport is observed between 5 and 7 Sv during January–March at 11°N. At 13°N it is significantly

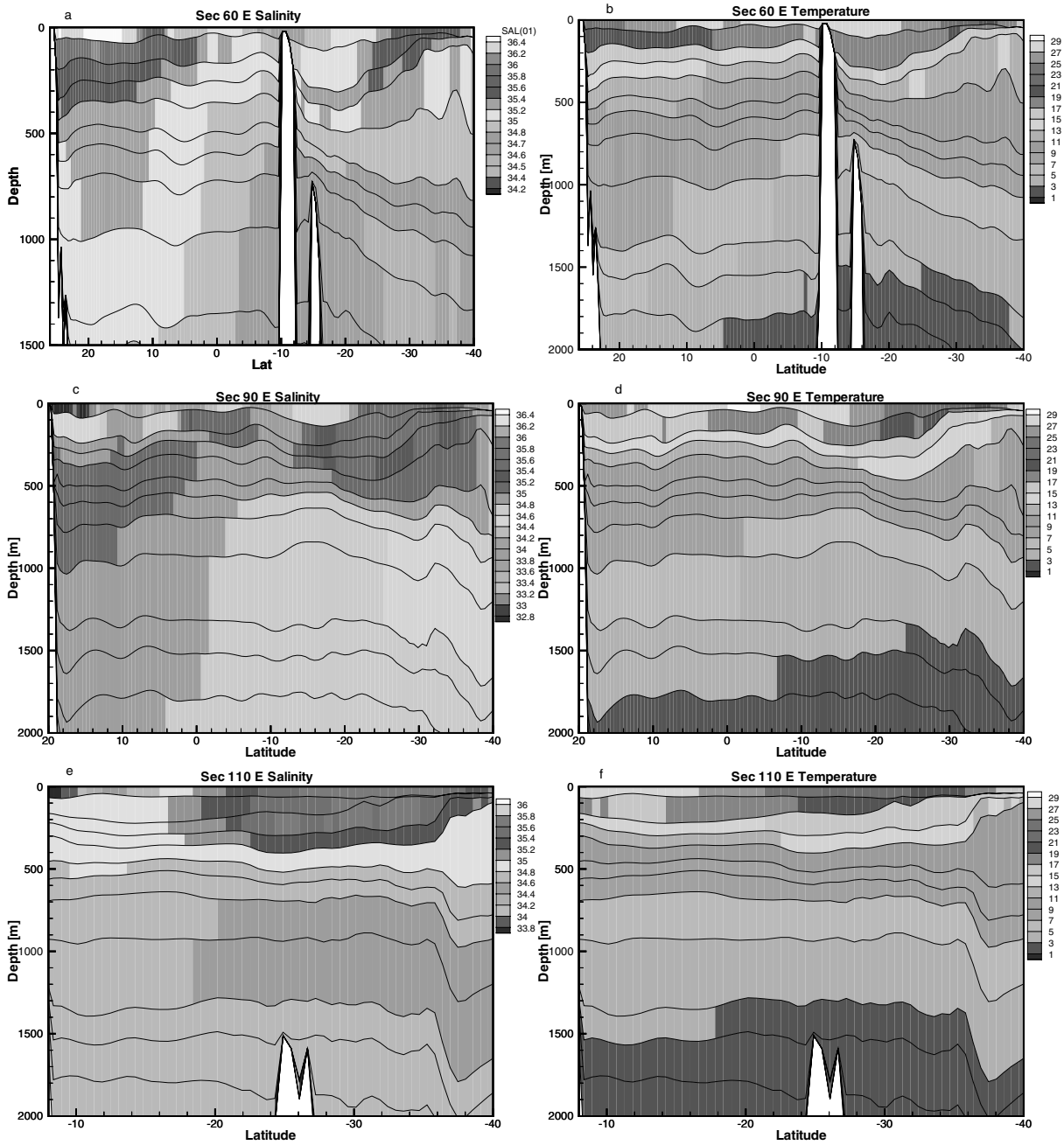

Figure 11. Meridional sections of monthly averaged salinity and temperature in the Indian Ocean during January 1996. The contour levels for the salinity have been chosen to best present the different salinity characteristics along the various sections. See color version of this figure at back of this issue.

stronger, above 5 Sv, and in 1993 and 1994 it was as high as 12–13 Sv in the upper 500 m, which is in good agreement with *Shetye et al.*'s [1996] hydrographic data, which shows a transport of 7.7 Sv. Our model results are also in agreement with *Shetye et al.* [1993], who found the EICC transport north of 13°N to vary between 2.6 and 7.1 Sv. The southward transport is strongest at 11°N, between 4 and 11 Sv in the upper 500 m. From hydrographic data a maximum northward transport of 10 Sv has been estimated in May at 16°N, and using a linear, continuously stratified model forced by Hellerman and Rosenstein winds, 5 Sv was simulated [*Shankar et al.*, 1996].

3.3.7. Western Indian Coastal Current. [41] The volume transport has also been calculated for the WICC, and its seasonal reversal is clearly observed from Figure 9. In the upper 10 layers (1500 m), between 5 and 10 Sv are transported north during the SW monsoon. Only ~1 Sv is confined in the surface layer. During the NE monsoon the flow is southward and weaker, ~2–5 Sv, except in 1997, when it was 6 Sv. We have no observation or model data to compare our results with.

3.4. Water Masses

[42] The model reproduces all the characteristic water masses in the Indian Ocean well at surface, intermediate, and deep layers. Meridional and zonal sections (Figure 1, dashed lines) of temperature and salinity have been plotted (only January 1996 is shown, as monthly changes are less significant in the deeper layers) to study the model's ability to reproduce the observed water masses in

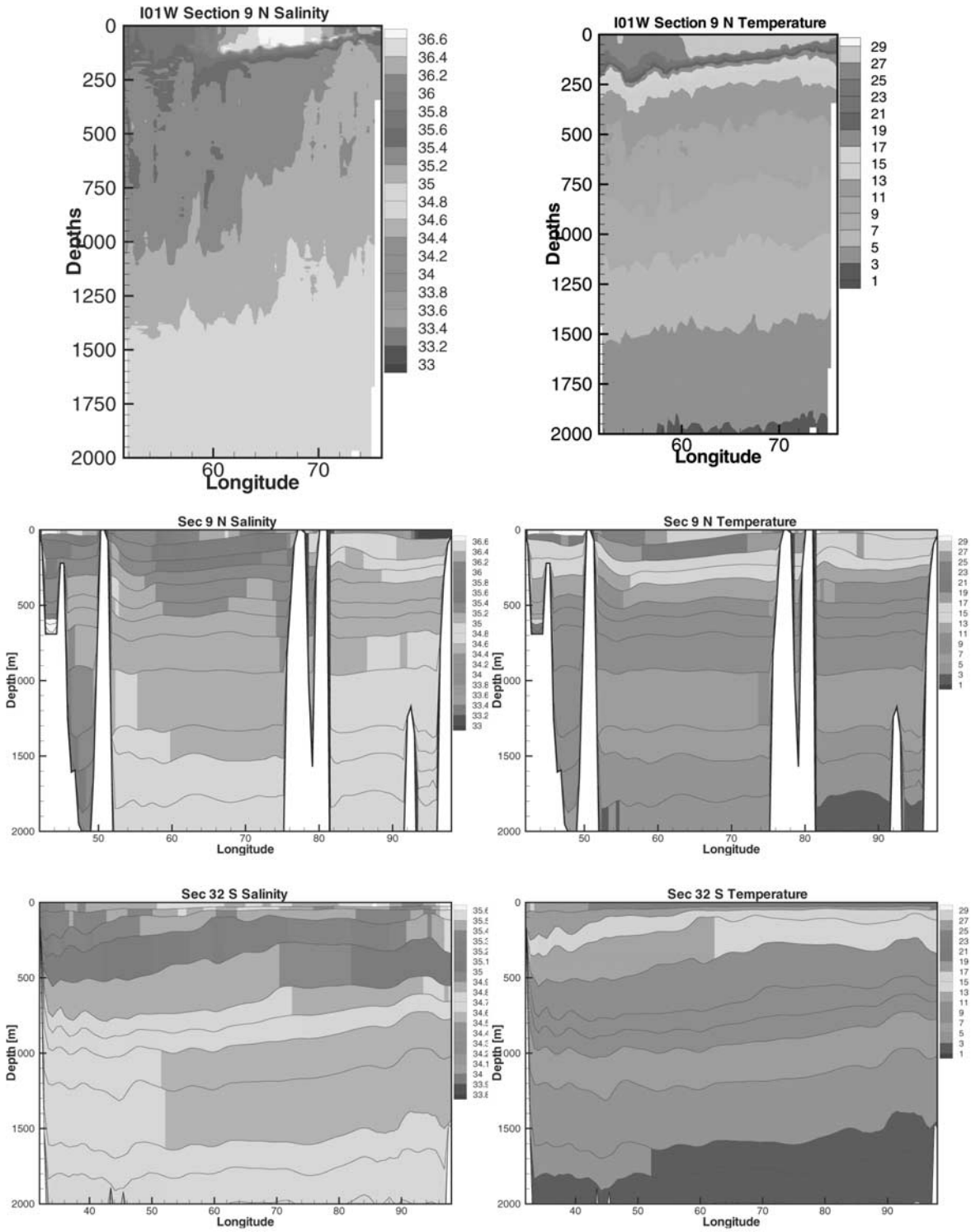

Figure 12. Zonal sections of monthly averaged (left) salinity and (right) temperature in the Indian Ocean. The contour levels for the salinity has been chosen to best present the different salinity characteristics along the various sections. (top) WOCE section along 9°N, (middle) simulated section along 9°N September 1995, (bottom) and simulated section along 32°S January 1996. See color version of this figure at back of this issue.

the Indian Ocean throughout a 6 year simulation. In addition, September 1995 is plotted for the section along 9° N since this is the period covered by World Ocean Circulation Experiment (WOCE) section I01W, one of the sections used for validation in this study. The major differences in temperature and salinity from month to month are observed in the surface. The sections have been validated using available in situ observations from *Wyrtki* [1971] oceanographic atlas from the Indian International Ocean

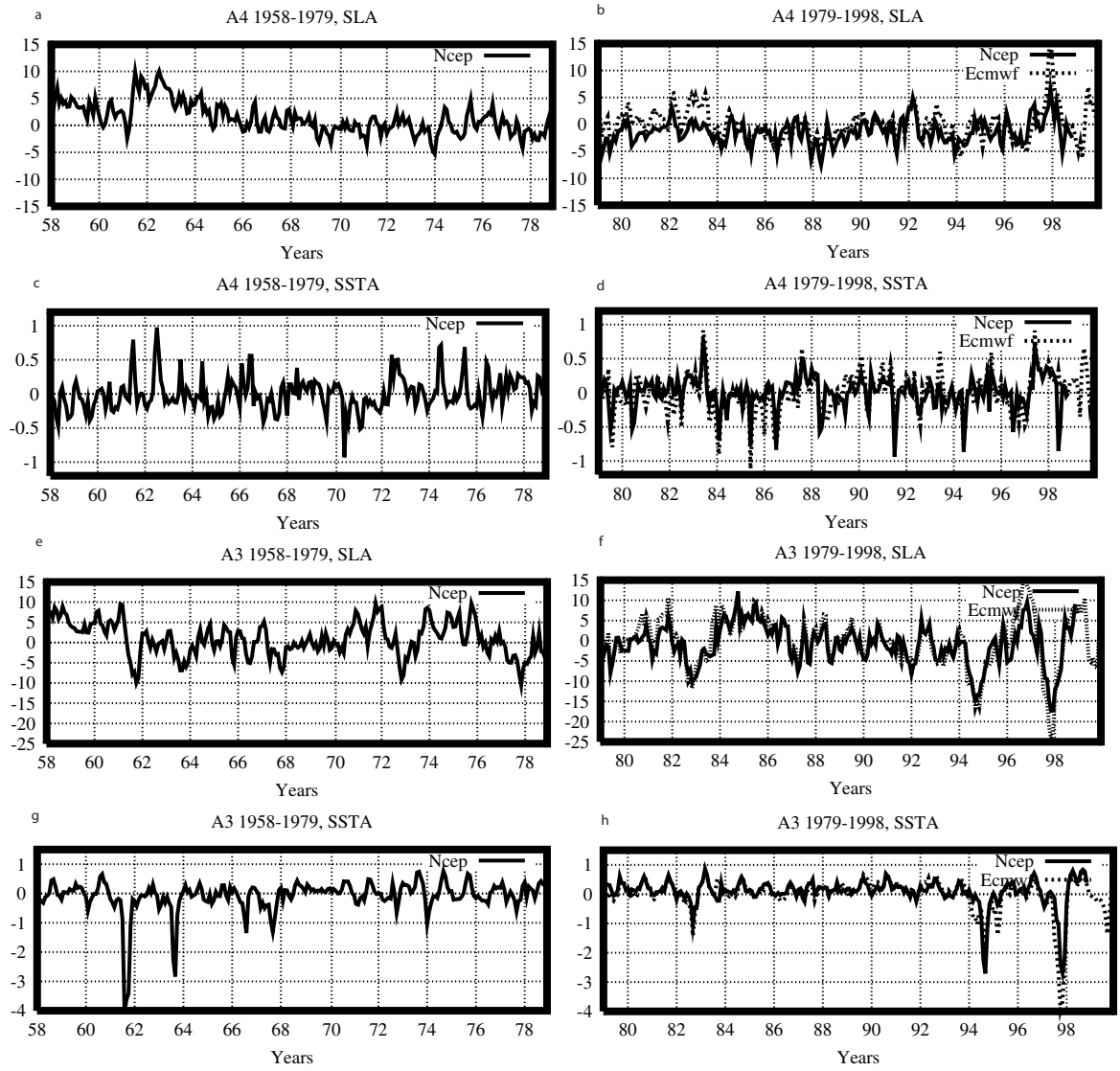

Figure 13. Timeseries of SLA (in cm) and SST (in degrees) in areas A4 (west Indian Ocean) and A3 (east Indian Ocean). Long-term mean and annual cycle have been removed.

Expedition (IIOE) and World Ocean Circulation Experiment data [*Schlitzer*, 2000] (also see http://sam.ucsd.edu/vertical-sections). In addition, the 32°S section has been validated using the *Toole and Warren* [1993] section conducted from the RRS *Charles Darwin* cruise during November–December 1987.

3.4.1. SSS and SST. [43] The sea surface temperature (SST) and sea surface salinity (SSS) monthly simulated mean distributions show consistent results for the 6 years (1992–1997) of synoptic simulation and are in good agreement with in situ data. Figure 10 shows the SST and SSS monthly simulated mean distribution for 2 months from this simulation, February and July 1996. The surface salinity map for February (Figure 10c) clearly demonstrates the westward penetration of the low-salinity water from the Bay of Bengal to the southern Arabian Sea, and salinities down to 33.7 psu are simulated off the southern coast of west India, consistent with in situ data.

[44] Near the south coast of Sri Lanka the WOCE Indian Ocean current meter mooring program 1991–1992 showed surface salinities down to 32 psu [*Schott et al.*, 1994], lower than the salinities of 33.0 psu simulated by MICOM. The low salinity suggests the origin of the water to be the northern Bay of Bengal from where it is presumably carried to Sri Lanka via the southwestern boundary current EICC. This difference is assumed to be due to the coarse model resolution and address the need to include more rivers in the Bay of Bengal to increase the freshwater input.

[45] In the southern Indian Ocean, surface salinities are generally high, in excess of 35.75 psu, along a band around 25°–35°S, reflecting the excess of evaporation over precipitation characteristics of the subtropics. Highest surface salinities of 36.01 psu in February are simulated in a small area at 85°E, 30°S, and lowest salinities, down to 35.25–35.3 psu, are simulated in the west just off the African coast, consistent with in situ data.

[46] North of the Subtropical Convergence, approximately at 30°S, most of the Indian Ocean surface water is tropical, having a uniformly high temperature between 25° and 29°C (Figure 10a), which corresponds well to *Reverdin and Fieux*'s [1987] results from XBT sections. On average, SST cools by 2°–3°C from May to September throughout most of the northern Indian Ocean, which is partly due to this area becoming cloudy and windy with the onset of the SW monsoon [*Godfrey et al.*, 1995]. Our simulations show a cooling in the SST by 2°–4°C from February (Figure 10a) to July (Figure 10b) in this area. In the Bay of Bengal the temperatures are lower, 26°–27°C during February, under the influence of the NE monsoon, than during the SW monsoon in July, 28°–29°C. Along

the Somali coast, particularly during July–August, the SST is low, <20°C (Figure 10a) as a result of upwelling.

3.4.2. Surface water masses 0–500 m. [47] In the northern Indian Ocean the Arabian Sea high-salinity water (ASW) mass and the low-salinity Bay of Bengal Water (BBW) have been simulated (Figure 11, sections 60°E and 90°E, and Figure 12, section 9°N). The ASW, with salinities up to 36.8 psu, is a mixture of Persian Gulf Water (PGW) and Red Sea Water (RSW) and results from excess of evaporation over precipitation in the Red Sea and Persian Gulf, both of which have similar salinities and temperatures. The main impact of these distributions is felt at intermediate levels. Once formed, it spreads southward and is simulated down to ~5°N with salinities of 35.2 to 36.8 psu and temperatures between 11° and 27°C (Figure 11, section 60°E), consistent with in situ data. These temperatures are lower than reported by *Rao and Griffiths* [1998], down to depths of 500 m, but compare well for the upper 100 m, which is consistent with *Kumar and Prasad*'s [1999] reported characteristics of the ASW. This low salinity causes the BBW to be separated from the water in the thermocline by a sharp halocline located between 50 and 100 m depth, restricting it to the surface layer. The WOCE I01W section (Figure 12, top) used for validating the 9°N section (Figure 12, middle) shows that the temperature is well simulated. The salinity also compares well; however, in the mixed layer the simulated salinity is ~0.2 psu less than seen from the WOCE data.

[48] In section 90°E (Figure 11) the decrease in salinity from 34.0 psu at 5°N to <31.0 psu in the northern part of the bay is seen. The BBW influence extends well into the tropics and is simulated down to 10°–15°S, which is in agreement with *Wyrtki* [1971] and WOCE data.

[49] In the equatorial region the Indonesian Upper Water (IUW) or Australasian Mediterranean Water (AAMW), the Indian Equatorial Water (IEW), and the South Indian Central Water (SICW) have been reproduced in our simulations (Figure 11, sections 60°E, 90°E and 110°E). IEW is observed between the ASW and SICW along section 60°E (Figure 11) between 5°N and 20°S, with salinities of 34.6–35.0 psu and temperatures between 8° and 25°C. AAMW is characterized by uniform salinity of ~34.8 psu or less, throughout the thermocline range [*You and Tomczak*, 1993]. From section 110°E (Figure 11) we observe the low-salinity BBW in the northern part of the section and the AAMW with salinities between 34.0 and 34.8 psu down to ~18°S, where it forms a strong gradient with the more saline SICW, with salinities up to 35.6 psu. Both these water masses have similar temperatures, between 8° and 23°C in the upper 600 m.

[50] Along section 32°S (Figure 12), SICW is simulated with temperatures between 9° and 23°C and salinities of 34.8–35.6 psu, with highest salinities observed in the western part of this section. *Toole and Warren* [1993] reported that at the African coast there is a shallow lens of water warmer than 20°C. This was also observed in the surface layer in our simulations along the whole 32°S section, in agreement with *Wyrtki*'s [1971] temperature plots.

3.4.3. Intermediate layer 500–1500 m. [51] The Red Sea and the Persian Gulf lie in an arid zone with low precipitation and high evaporation, resulting in high temperature and high salinity in excess of 40 psu in the northern part. The RSW and PGW supply water to intermediate depths ranges owing to their high densities and form a salinity maximum at depths between 600 and 900 m, with a temperature of 11°C and salinities of 35.5–35.7 psu. In the Arabian Sea (section 60°E, Figure 11) and in the Bay of Bengal (section 90°E, Figure 11) the Red Sea Persian Gulf Intermediate Water (RSPGIW) is simulated down to 5°S with salinities between 34.8 and 35.3 psu and temperatures between 5° and 13°C. The southern boundary, which extends down to 5°S in the Arabian Sea, mixes with the Antarctic Intermediate Water (AAIW) down to 15°S. Water masses are simulated with salinities of 34.6–34.8 psu, which lies between the characteristics of RSPGIW and AAIW. In the Bay of Bengal the southern boundary mixes with Indonesian

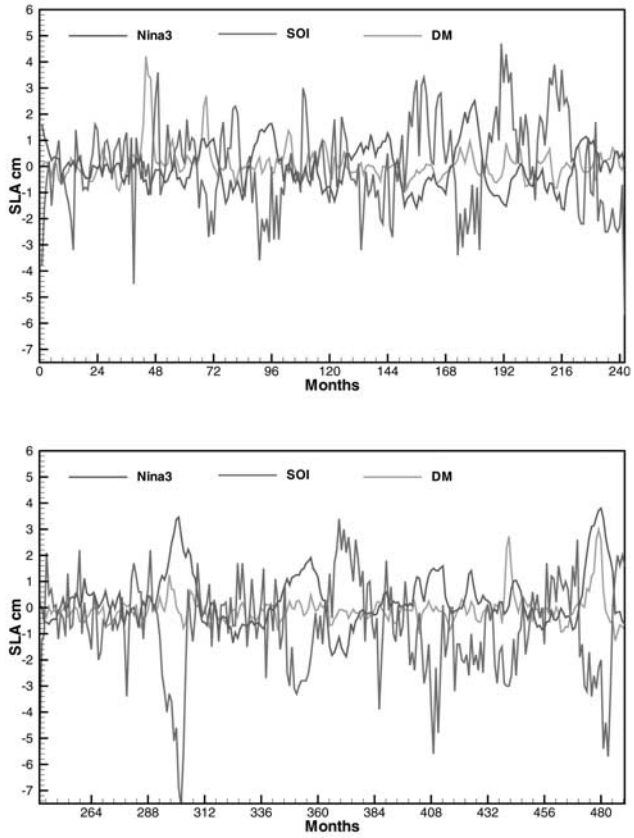

Figure 14. Dipole mode calculated for simulated SSTA, Southern Oscillation Index (SOI), and Nina3 for 1958–1998. SOI gives a measure of the strength and phase of the Southern Oscillation and indicates the status of the Walker circulation. Nina3 represents the El Niño in the Pacific Ocean from SSTA of the central and eastern equatorial Pacific. See color version of this figure at back of this issue.

Intermediate Water (IIW), which is identified along section 90°E (Figure 11) between 5° and 20°S, with salinities of 34.6–34.7 psu and temperatures between 3° and 9°, indicating traces of RSPGIW.

[52] In section 110°E (Figure 11), IIW is identified north of 20°S, with salinities between 34.4 and 34.7 psu and temperatures between 3° and 6°C, also in excess of those reported by *Rao and Griffiths* [1998]. The low-salinity signature, 33.8–34.6 psu, of AAIW is well developed along section 32°S (Figure 12). Salinities of 34.4–34.5 psu are simulated up to 15°–18°S, and continue to increase farther north. Highest AAIW layer salinities were found in the west. Along section 90°E (Figure 11), AAIW is observed south of 25°S, and in section 110°E (Figure 11) it is observed up to 18°S. AAIW is prevented from entering the Northern Hemisphere by the equatorial current system north of 10°S [*Rao et al.*, 1989]. At its source in the Atlantic it has a temperature of 2°–2.5°C and salinity of 33.8 psu, but when it enters the subtropical gyre, its temperature increases to 3°–4°C, and its salinity increases to 34.3 psu.

3.4.4. Below 1500 m. [53] Below depths of 1500 m the Circumpolar Deep Water (CDW) has been simulated, with salinities between 34.6 and 34.75 psu. Corresponding temperatures range between 0° and 4°C, slightly higher than reported by *Rao and Griffiths* [1998]. Salinities as high as 34.73 psu have been observed along section 32°S. This attenuates northward and reaches a minimum at 20°S of ~34.5–34.6 psu. It then increases somewhat to the north because of the vertical flux, and along the 10°N section, values up to 34.8 psu are simulated.

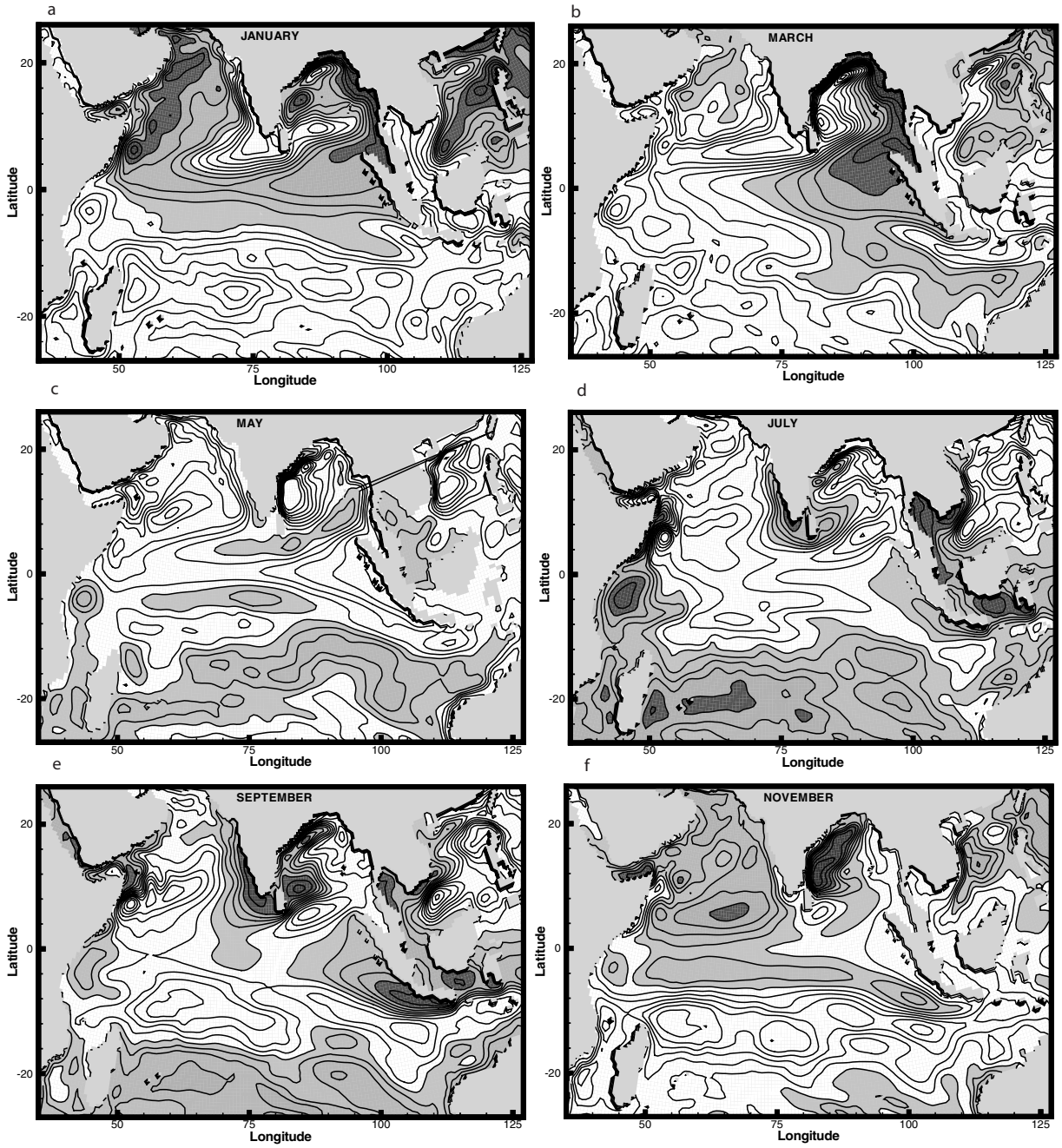

Figure 15. Monthly averaged SLA (in cm) over 40 years. Every second month is shown. Negative anomalies are shaded. Contour interval is 2 cm.

[54] We conclude that the simulation of SLA, the surface circulation, volume transport, and water masses in the surface and deeper layers using MICOM is good. We therefore with confidence use this model to further study the interannual variability during 1958 to 1999, which is done in section 4.

4. Ocean Variability 1958–1998: A Numerical Experiment

[55] The ocean variability and the interannual signals in the Indian Ocean are investigated by simulating SLA and sea surface temperature anomalies over a 40 year model integration using NCEP forcing fields. Previous studies [*Webster et al.*, 1999; *Saji et al.*, 1999] have led to the recognition of the Indian dipole mode. However, investigators have mainly focused their attention on the last and strongest El Niño event in 1997 [*Webster et al.*, 1999; *Yu and Rienecker*, 2000]. *Murtugudde et al.* [2000] studied the oceanic process associated with anomalous events in the Indian Ocean and performed a 40 year simulation using a sigma layer model, but his attention was also focused on the 1997 event.

[56] In addition, a 20 year integration has been performed over the last 20 year period using ECMWF forcing (1979–1999) for

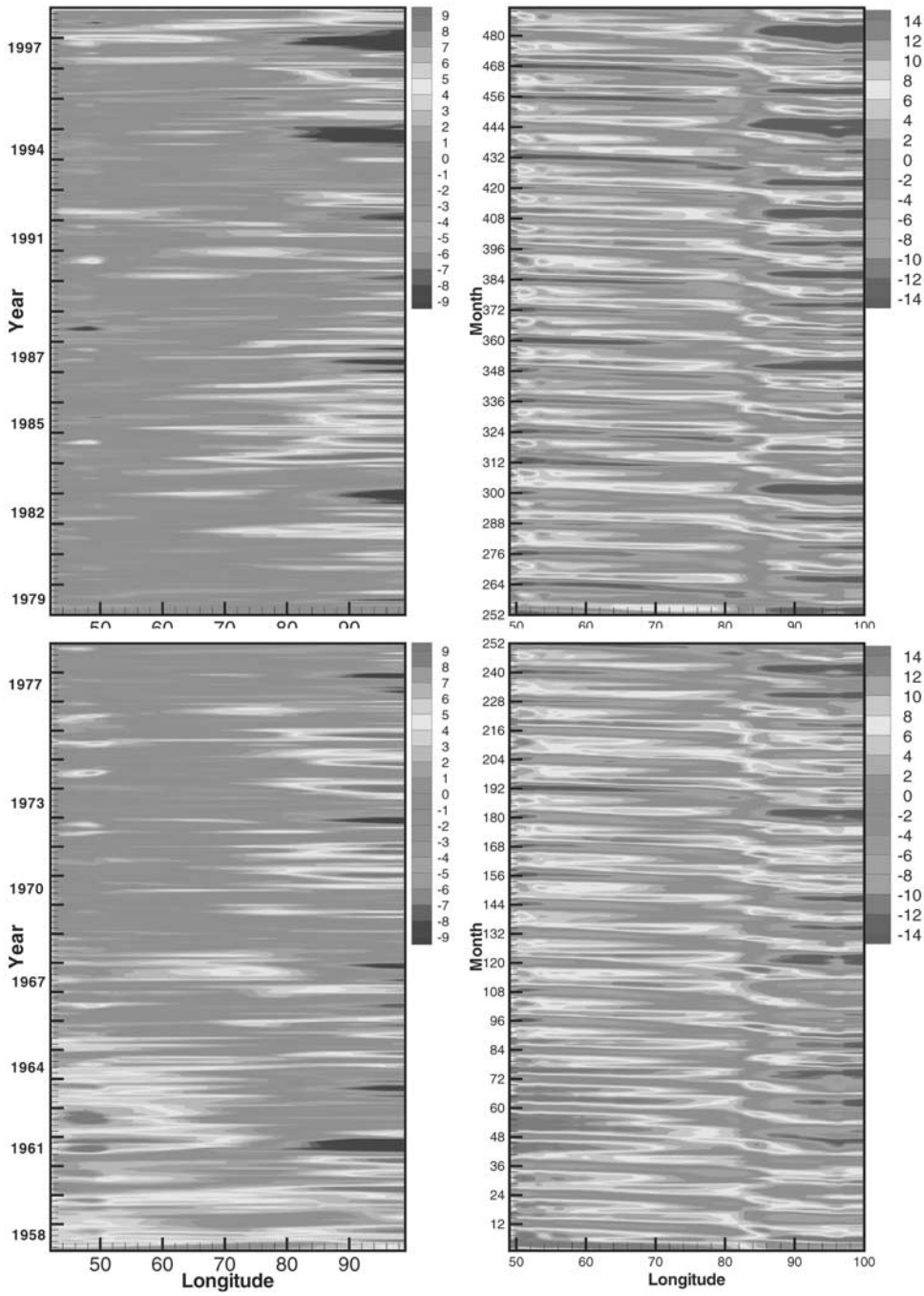

Figure 16. Hovmöller plots for SLA (in cm) for the 40 year simulation using NCEP forcing averaged (left) over 2°N and 2°S (right) and between 4° and 6°N. See color version of this figure at back of this issue.

comparison to NCEP forcing fields to see if significant different responses exist from these two forcing fields. If no significant difference is observed (to be discussed below), we feel confident in using the longer times series of NCEP.

[57] Time series of SSTA and SLA averaged over several smaller areas in the model domain were compared for the 20 years (1979–1998) of common integration using ECMWF and NCEP forcing fields (Figure 13). In general, SLA averaged over different areas show higher amplitudes using ECMWF compared to NCEP (Figures 13b and 13f). The simulation using ECMWF forcing fields show warmer SSTA of the order of 0°–0.2°C compared to the simulation using NCEP forcing (Figures 13d and 13h). Greatest differences are seen in the eastern averaged area, A3 (95°–105° E, 10°S–0°N) (Figure 1). In 1997, SSTA from the integration using ECMWF forcing were 1.5°C colder than with NCEP forcing (Figure 13h). However in 1983 and 1994, NCEP shows SSTA 1.0°C colder than ECMWF. In the western area A4 (45°–55°E, 5°S–5° N) (Figure 1), differences between the anomalies are less (Figure 13d). Overall, SSTA is simulated warmer using ECMWF forcing fields. Differences of

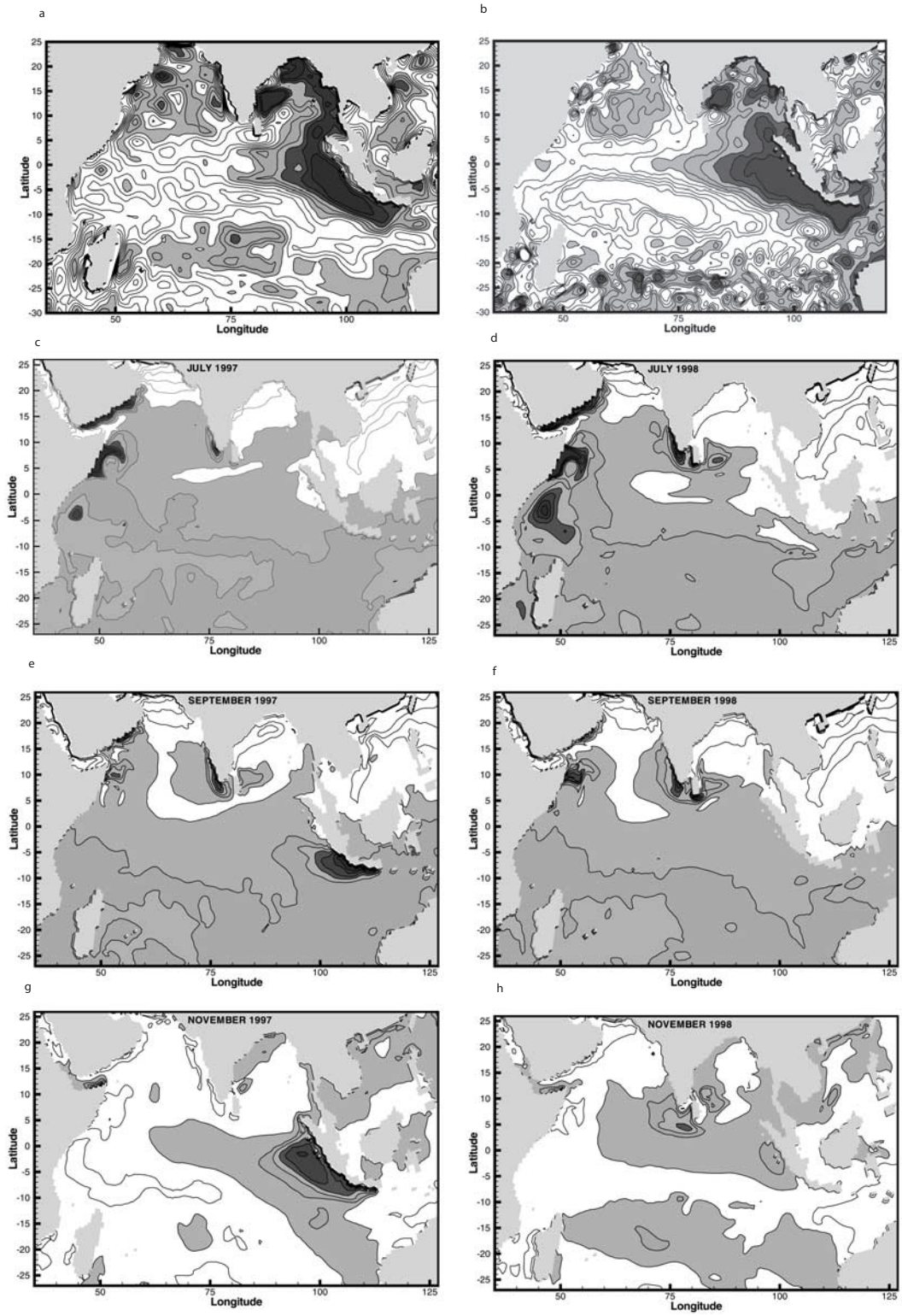

Figure 17. Monthly averaged SLA and SSTA. (a) Simulated SLA for November 1997 and (b) observed SLA for November 1997. (c–f) SSTA for a unusual year, 1997 (Figures 17c, 17e, and 17g), and a normal year, 1998 (Figures 17d, 17f, and 17h), for July, September, and November. Negative anomalies are shaded. Only long-term mean has been removed. Contour interval is 1°.

almost 1°C are observed in 1980, 1991, 1993, 1995, and 1998, where NCEP shows coldest anomalies (Figure 13d). The usage of different forcing fields clearly affects SSTA (0°–1°) less than SLA (0–7 cm), a likely reason being the use of temperature relaxation at the surface. We can conclude that the significance of using one forcing compared to the other is, in general, little, and we can therfore use the NCEP forcing in the 40 year simulation.

4.1. Temporal Evolution

[58] From the PCA, only the dominant mode which describes the annual signal accounting for 40.3 and 81.0% of the variance for SLA and SSTA respectively, is shown (Figures 2a and 2b). Strongest SLA and SSTA are observed during the SW monsoon, with peaks in July, indicating high mesoscale activity. Every 4 years, starting in 1960, a warming at the beginning of the year is observed (amplitude reduced for negative SSTA). This 4 year signal, not previously reported, only seen from SSTA and not from SLA, has not been identified, although some of the years coincide with La Niña years. In addition, an increase in SLA coincides with years previously been identified as El Niño years in the Pacific Ocean and will be discussed in section 4.3.3.

[59] The dominant mode for zonal ECMWF wind stress also describes the annual signal, which accounts for 55.7% of the variance, with peaks during the SW monsoon. Figure 2c shows a time lag <2 months between the peak of the zonal wind stress and the peak of the SLA using ECMWF forcing. This, we assume, is the ocean's response time, which is in agreement with *Johannessen et al.*'s [1981] results. A reduction in zonal wind stress results in a reduction in SLA between 0 and 2 months later during years which have been identified as El Niño years.

4.2. Kelvin and Rossby Waves

[60] One of the characteristic features of the equatorial region is the presence of Rossby and Kelvin waves. In the Indian Ocean, during the NE monsoon, upwelling Kelvin waves and downwelling Rossby waves, which are seen as negative and positive SLA, respectively [*Cipollini et al.*, 1998], are generated at the equator due to the strong northeasterlies. In all oceans, Kelvin waves travel east along the equator, hit the coast, and reflect back as westward propagating Rossby waves. Kelvin waves are very fast traveling waves and are difficult to observe. However, along the equatorial section between days 320–400 and 720–800 (Figure 4c), the positive SLA observed from both altimeter and model data over the whole Indian Ocean are thought to indicate these Rossby waves. They have a phase speed of 140–230 cm/s, which is in agreement with *Yang et al.* [1998]. Some of the energy of the Kelvin waves may move along the eastern coast as two coastal Kelvin waves, one northward and one southward. This signal can be found propagating the entire coastline around the Bay of Bengal and reaches the east coast of India about a month later.

[61] In the Indian Ocean, Rossby waves near the eastern boundary off Sumatra can be generated either locally by along shore winds or remotely by reflection of equatorial Kelvin waves [*Yang et al.*, 1998]. In January and February (Figures 14, top, and 15a), negative SLA are simulated at equator and in the eastern basin, and positive SLA are observed off both coasts of India. In March, (Figure 15b), upwelling Rossby waves are radiated offshore from the eastern boundary, and downwelling Rossby waves are observed at the western boundary. To confirm that these positive and negative anomalies are Kelvin or Rossby waves, Hovmöller plots are used. From Figure 16b, along 5°N we confirm these anomalies to be westward propagating Rossby waves. In the southern Indian Ocean between 10° and 20°S, downwelling Rossby waves (positive SLA) dominate during the NE monsoon (September to April), and upwelling Rossby waves (negative) SLA dominate during the SW monsoon.

[62] The abrupt change in the wind direction along the equatorial region during April–May causes a change in the upper ocean, depressions in the thermocline, and a rise in the ocean surface, which triggers eastward propagating downwelling Kelvin waves [*Yang et al.*, 1998]. This deepening of the thermocline is well simulated by the model but not shown.

[63] After the coastally trapped Kelvin waves reach the coast of India, they radiate westward propagating downwelling Rossby waves to the interior of the Arabian Sea, which reach the Somali coast in March–April (Figure 15b), taking ~3–4 months. This is also seen as a discontinuity at 80°E around days 300–360 and 600–660 (December–April) in Figure 4 along the 5° N section, which indicates these downwelling Rossby waves (positive SLA) at both sides of India. The southward wind along the west coast of India during the NE monsoon forces these upwelling Rossby waves.

[64] With the start of the SW monsoon, downwelling Kelvin waves are excited. In May (Figure 15c), simulated downwelling Kelvin waves have reached the eastern boundary, and downwelling Rossby waves are being radiated offshore (Figure 15b). In June, negative anomalies off both coasts of India are simulated (also seen in Figure 15d for July). These upwelling Rossby waves are radiated into the Arabian Sea from the west coast of India and reach the Somali coast in October–November (Figures 15f and Figure 16b).

[65] From July to October (Figures 15d and 15e), upwelling waves (negative SLA) are clearly seen in the eastern basin. The only mechanism for forcing such waves is the easterly wind between May and September in the central equatorial basin [*Yang et al.*, 1998]. In the central equatorial basin the zonal wind becomes westerlies between September and November, and we simulate downwelling waves forced by this change near the eastern boundary in November–December (Figure 15f).

[66] Rossby phase speeds are calculated from Figure 4 and are of the order of 24–26 cm/s at 5°N and 5°S, which is slightly lower than the 30 cm/s computed from the *Killworth et al.* [1997] theory. At 10°N and 10°S, speeds are observed to be ~14 cm/s, and they are observed to be 11–13 cm/s at 15°N, which is in agreement with the *Killworth et al.* [1997] theory.

4.3. ENSO Events

[67] From time series of SLA and SSTA (long-term and annual mean removed) for the 40 year simulation we identify several years with unusual cooling in the east and warming in the west, which coincide with a negative Southern Oscillation Index (SOI) and El Niño years, which will be discussed in section 4.3.3. In addition, we have looked at the influence of the upwelling off the southwest coast of India with these years.

4.3.1. Eastern part. [68] Time series of SLA and SSTA in area A3 (Figures 13e–13h) together with Hovmöller plots of SLA averaged over 2°N–2°S (Figure 16a) is used to examine more closely the eastern part where unusual cooling and high negative SLA are observed throughout the model integrations. High negative SLA are identified during the years 1961, 1963, 1966–1967, 1972, 1977, 1982, 1987, 1991–1992, 1994, and 1997 (Figures 13e, 13f, and 16a). These negative anomalies first appear in June off Sumatra. Since a significant drop in SLA off the coast of Sumatra suggests increased upwelling of cold deep water, Figure 17c, which shows monthly averaged SSTA, can illustrate the above. SLA increases and penetrates northwestward (November seen in Figure 17a) before they start to decay in December and last until March the following year (Figure 16). SLA above 20 cm are observed in 1961, 1982, and 1994, and between November 1997 and May 1998 they exceed 30 cm (Figure 17a). This is in agreement with our altimeter results (Figure 17b) and also with *Webster et al.* [1999].

[69] Cooling is simulated off Sumatra during June with the drop in SLA (also seen in July in Figure 17). During the following months this cooling intensifies and migrates toward the equator along the Indonesian coastline (Figures 17c, 17e, and 17g). Extreme cooling, averaged over area A3, is simulated in 1961, 1963, 1966–1967, 1982, 1994, and 1997 (Figures 13e and 13f). The strongest events indicate a cooling of 3°–4°C. A peak of SSTA normally occurs in October–November followed by a rapid decrease in December. However, this varies slightly from event to event. During October–November 1982, for example, the cooling is less compared to November–December 1987, and its

spatial coverage is less together with an earlier retreat. Monthly averaged SSTA (Figure 17) from an extreme year (1997) and a normal year (1998) illustrate the cooling during July, September, and November. From the Hovmöller plot a cooling of 7°C off Sumatra was simulated in September, which decreased to 5.5°C in December.

[70] With the extreme cooling the mixed layer reduces to <30 m (not shown), and the salinity increases by 0.1–0.3 psu (not shown). Strongest increases in SST, with salinities between 34.3 and 34.4 psu, are simulated at the times of extreme cooling. In this area the very fresh Bay of Bengal Water is only confined to the upper layer, and thus, when upwelling occurs, more saline water is brought to the surface. The extreme cooling as described above is followed by a next year warming observed during 1973, 1983, 1996, and 1998 (some of these are seen in Figures 13e and 13f), of which some coincide with La Niña in the Pacific Ocean.

4.3.2. Western part. [71] At the same time as the cooling in the east, the western Indian Ocean experiences a warming of 0.5°–1°C, with greatest amplitudes during 1961, 1962, 1966, 1974, 1975, 1983, 1987, 1991, 1995, and 1997 (Figures 13c, 13d, and 16). Figure 17 shows the difference between an extreme year (1997) and a normal year (1998), and we observe a warming of 1°C during unusual years. The warming in this area is more significant using ECMWF forcing, which simulates a warming of ~2°C (not shown).

[72] With this warming, SLA increases, and higher than normal positive SLA are simulated during the years 1961–1962, 1982, 1992, and 1997–1998 (Figures 13a and 13b). Between 5° and 12°S, there is an elongated "ridge" with amplitudes above 25 cm in November 1997 (Figure 17), extending between the coast of Africa and almost across the whole Indian Ocean, tilting slightly southeast. This ridge was also identified by *Webster et al.* [1999], who concluded that the location and magnitude of the ridge are consistent with Ekman convergence due to southward Ekman flow at the equator (from easterly winds) and northward flow at 10°S (from westerlies). In 1982 it is located in the central Indian Ocean, covering a much smaller area compared to the SLA simulated during the 1997 event. The same phenomenon was also simulated in 1986, 1991, and 1994 (not shown). Hovmöller plots of this ridge suggests that it is westward propagating Rossby wave. The mixed layer also increases by almost 20 m and reaches a depth between 70 and 75 m (not shown).

4.3.3. Link to ENSO. [73] To further investigate any possible relationship between the extreme events observed in the Indian Ocean, the dipole mode index (DMI) was calculated by computing the difference between SSTA in areas A4 and A3 and plotted with the SOI and Nina3 (Figure 14). The DMI is clearly related to ENSO during most of the extreme years. However, the DMI is weaker than the Nina3 cycle, and there also seems to be some time lag between the two events. SOI is negative when DMI and Nina3 are positive, which is associated with El Niño. However, in 1961 we have a strong unusual event in the Indian Ocean at the end of the year. This is not an El Niño year. However, in 1961, SOI is negative at the beginning of the year, so there is some possible relationship between SOI and DMI also during this year. This leads us to conclude that the DMI for the Indian Ocean coincides with El Niño, as observed in the Pacific Ocean, except for 1961.

4.3.4. Southwest coast of India. [74] The southwest coast of India is a region which experiences upwelling of cold nutrient water from the end of May until November (Figure 7). The model simulates this upwelling with a peak during August, and our results agree well with *Johannessen et al.* [1981]. The offshore movement of surface water leads to a lowering of sea level toward the coast. Cold upwelled water, <20°C, is normally transported into the Bay of Bengal during the summer by the Indian Monsoon Current (IMC). During El Niño years the westerlies are weaker than during normal years, and hence the IMC weakens, and gyres in the southern part of the bay weaken. In 1958, 1961, 1964, 1972, 1974–1975, 1985, 1988, 1992, and 1997, years associated with El Niño, the inflow of cold water into the Bay of Bengal was reduced (not shown). Less upwelling off the coast of southwest India was also simulated. Years 1988 and 1997 experienced the longest reduction, and 1997 had the strongest event, with upwelling only simulated between July and September (not shown). Again, we can see a strong correlation with ENSO events apart from 1961.

5. Conclusion

[75] The MICOM has been implemented and validated and used in a multi year simulation forced by synoptic atmospheric data to get a better understanding of the monsoon circulation in the Indian Ocean. The model is more complete and complex than previous model studies and has proven to reproduce the general ocean circulation, water masses and the volume transports for selected currents well when compared to observations and previous model results. We have also shown that the influence of the monsoon is confined to the upper 300–500 m for the Indian Monsoon Current and the Northeast Monsoon Current. Further, the model was capable of simulating SLA and the monsoon characteristics in good agreement with altimeter data. High correlation is observed along the equator, in the southeastern and northern Indian Ocean, but not in the interior of the Bay of Bengal. Correlation is less close to land (which might be due to the altimeter near-shore errors) and in high-variability areas, indicating that the present model resolution is too coarse for resolving all the mesoscale features seen by the altimeter data. There seems to be a time lag of 1–4 weeks before the ocean responds to the monsoon winds. In the southern Bay of Bengal a cyclonic gyre G4 (Figure 7), forced by the Indian Monsoon Current and previously unknown, has been validated and discussed. This gyre is clearly influenced by the strength of the Indian Monsoon Current.

[76] On the basis of the positive model validation a 40 year integration was performed to investigate interannual variability. Since the validation was performed using ECMWF data, we found it necessary to investigate the models sensitivity to atmospheric forcing. There were a few small differences, but we can with confidence use the longer time simulation using the 40 year NCEP forcing fields.

[77] Propagation of equatorial waves caused an extreme cooling as high has 4°C off Indonesia, in the eastern part of the Indian Ocean, and warming in the west, off Somalia, during years which coincide with negative SOI. These years, except 1961, coincide with Pacific Ocean El Niño years. The cooling off Indonesia is normally followed by a warming the following year. Reduced upwelling off the coast of India and less inflow of cold water into the Bay of Bengal are associated with El Niño years. Therefore we conclude that El Niño events occur very clearly in the Indian Ocean.

[78] **Acknowledgments.** V. E. J. Haugen is supported by the Norwegian Research Council Ph.D. Fellowship program under contract 129247/730. This work has received support from a grant of CPU time from the Norwegian supercomputing community (TRU) through a grant of computer time.

References

Anderson, D., D. Carrington, R. Corry, and C. Gordon, Modelling the variability of the Somali Current, *J. Mar. Res.*, *49*, 659–696, 1991.

Antony, M., Northward undercurrent along west coast of India during upwelling—Some interferences, *Ind. J. Mar. Sci.*, *19*, 95–1015, 1990.

Babu, V. R., V. Murty, L. Rao, C. Prabhu, and V. Tilvi, Thermohalin structure and circulation in the upper layers of the southern Bay of Bengal during BOBMEX–Pilot (October–November 1998), *Ind. Acad. Sci*, *109*, 255–265, 2000.

Bentsen, M., G. Evensen, H. Drange, and A. Jenkins, Coordinate transformation on a sphere using conformal mapping, *Mon. Weather Rev.*, *127*, 2733–2740, 1999.

Bleck, R., and D. Boudra, Wind-driven spin-up in eddy-resolving ocean models formulated in isopycnic and isobaric coordinates, *J. Geophys. Res.*, *91*, 7611–7621, 1986.

Bleck, R., and L. Smith, A wind-driven isopycnic coordinate model of the North and equatorial Atlantic Ocean, 1, Model development and supporting experiments, *J. Geophys. Res.*, *95*, 3273–3285, 1990.

Bleck, R., H. Hanson, D. Hu, and R. Kraus, Mixed layer-thermocline interaction in a three-dimensional isopycnic coordinate model, *J. Phys. Oceanogr.*, *19*, 1417–1439, 1989.

Bleck, R., D. H. C. Rooth, and L. Smith, Salinity-driven thermocline transients in a wind- and thermohaline-forced isopycnic coordinate model of the North Atlantic, *J. Phys. Oceanogr.*, *22*, 1486–1505, 1992.

Bruce, J., The wind field in the western Indian Ocean and the related ocean circulation, *Mon. Weather Rev.*, *111*, 1441–1452, 1983.

Bruce, J., D. Johnson, and J. Kindle, Evidence for eddy formation in the eastern Arabian Sea during the northeast monsoon, *J. Geophys. Res.*, *99*, 7651–7664, 1994.

Bruce, J., J. Kindle, L. Kantha, J. Kerling, and J. F. Baily, Recent observations and modeling in the Arabian Sea Laccadive High region, *J. Geophys. Res.*, *103*, 7593–7600, 1998.

Cipollini, P., D. Cromwell, and G. Quartly, Observations of Rossby wave propagation in the northeast Atlantic with TOPEX/Poseidon altimetry, *Adv. Space Res.*, *22*(11), 1553–1556, 1998.

Cutler, A., and J. Swallow, Surface currents of the Indian Ocean: Compiled from historical data archived by the meteorological Office, Bracknell, UK, *Rep. 187*, Inst. of Oceanogr., Wormley, England, 1984.

Fischer, J., F. Schott, and L. Stramma, Currents and transports of the Great Whirl-Socotra Gyre system during the summer monsoon, August 1993, *J. Geophys. Res.*, *101*, 3573–3587, 1996.

Gaspar, P., Y. Gregories, and J.-M. Lefevre, A simple eddy kinetic energy model for simulations of the oceanic vertical mixing: Tests at station Papa and long-term upper ocean study site, *J. Geophys. Res.*, *95*, 16,179–16,193, 1990.

Godfrey, J., et al., The role of the Indian Ocean in the global climate system: Recommendations regarding the global ocean observing system, *Background Rep. 6*, Ocean Obs. Syst. Dev. Panel, Tex. A & M Univ., College Station, 1995.

Hastenrath, S., and L. Greischar, The monsoonal current regime of the tropical Indian Ocean: Observed surface flow fields and their geostrophic and wind-driven components, *J. Geophys. Res.*, *96*, 12,619–12,633, 1991.

Hellerman, S., and M. Rosenstein, Normal monthly wind stress over the World Ocean with error estimates, *J. Phys. Oceanogr.*, *13*, 1093–1104, 1983.

Hurlburt, H. E., and J. D. Thompson, A numerical model of the Somali Current, *J. Phys. Oceanogr.*, *6*, 646–664, 1976.

Jensen, T., Equatorial variability and resonance in a wind-driven Indian Ocean model, *J. Geophys. Res.*, *98*, 22,533–22,552, 1993.

Johannessen, O. M., G. Subbaraju, and J. Blindheim, Seasonal variations of the oceanographic conditions off the southwest coast of India during 1971–1975, *Fiskfir. Skr. Ser. Havunders.*, *18*, 247–261, 1981.

Killworth, P., D. Chelton, and R. D. Szoeke, The speed of observed and theoretical long extratropical planetary waves, *J. Phys. Oceanogr.*, *27*, 1946–1966, 1997.

Kumar, S. P., and T. G. Prasad, Formation and spreading of Arabian Sea high salinity water mass, *J. Geophys. Res.*, *104*, 1455–1464, 1999.

Legates, D., and C. Willmott, Mean seasonal and spatial variability in gauge-corrected, global precipitation, *J. Clim.*, *10*, 111–127, 1990.

Le Traon, P.-Y., Basin-scale oceanic circulation from satellite altimetry, in *Oceanographic Applications of Remote Sensing*, edited by M. Ikeda and F. Dobson, pp. 79–96, CRC Press, Boca Raton, Fla., 1995.

Le Traon, P.-Y., and F. Ogor, ERS-1/2 orbit improvement using TOPEX/Poseidon: The 2 cm challenge, *J. Geophys. Res.*, *103*, 8045–8057, 1998.

Le Traon, P.-Y., F. Nadal, and N. Ducet, An improved mapping method of multisatellite altimeter data, *J. Atmos. Ocean. Technol.*, *15*, 522–534, 1998.

Levitus, S., and T. P. Boyer, *World Ocean Atlas 1994*, *Temperature, NOAA Atlas NESDIS 4*, vol. 4, Natl. Oceanic and Atmos. Admin., Silver Spring, Md., 1994.

Levitus, S., R. Burgett, and T. P. Boyer, *World Ocean Atlas 1994 Salinity, NOAA Atlas NESDIS 3*, vol. 3, Natl. Oceanic and Atmos. Admin, Silver Spring, Md., 1994.

McCreary, J., W. Han, D. Shankar, and S. Shetye, Dynamics of the East India Coastal Current, 2, Numerical solutions, *J. Geophys. Res.*, *101*, 13,993–14,010, 1996.

Molinari, R., D. Olson, and G. Reverdin, Surface current distributions in the tropical India Ocean derived from compilations of surface bouy trajectories, *J. Geophys. Res.*, *95*, 7217–7238, 1990.

Murtugudde, R., J. P. McCreary Jr. and A. Busalacchi, Oceanic processes associated with anomalous events in the Indian Ocean with relevance to 1997–1998, *J. Geophys. Res.*, *105*, 3295–3306, 2000.

Perry, G., P. Duffy, and N. Miller, An extended data set of river discharges for validation of general circulation models, *J. Geophys. Res.*, *101*, 21,339–21,349, 1996.

Potemra, J., M. Luther, and J. O'Brian, The seasonal circulation of the upper ocean in the Bay of Bengal, *J. Geophys. Res.*, *96*, 12,667–12,683, 1991.

Preisendorfer, R., *Principal Component Analysis in Meteorology and Oceanography*, Elsevier Sci., New York, 1988.

Rao, R., R. Molinari, and J. Festa, Evolution of the climatological near-surface thermal structure of the tropical Indian Ocean, 1, Description of mean monthly mixed layer depth, and sea surface temperature, surface current, and surface meteorological fields, *J. Geophys. Res.*, *94*, 10,801–10,815, 1989.

Rao, T. S. S., and R. C. Griffiths, *Understanding the Indian Ocean: Perspectives on Oceanography*, United Nations Educ., Sci., and Cultural Org., Paris, France, 1998.

Reppin, J., F. Schott, J. Fischer, and D. Quadfasel, Equatorial current and transport in the upper central Indian Ocean: Annual cycle and interannual variability, *J. Geophys. Res.*, *104*, 15,495–15,514, 1999.

Reverdin, G., The upper equatorial Indian Ocean: The climatological seasonal cycle, *J. Phys. Oceanogr.*, *17*, 903–927, 1987.

Reverdin, G., and M. Fieux, Sections in the western Indian Ocean—Variability in the temperature structure, *Deep Sea Res.*, *34*, 601–626, 1987.

Saji, N., B. Goswami, P. Vinayachandran, and T. Yamagata, A dipole model in the tropical Indian Ocean, *Nature*, *401*, 360–363, 1999.

Schlitzer, R., Electronic atlas of WOCE hydrographic and tracer data now available, *Eos Trans. AGU*, *81*(5), 45, 2000.

Schott, F., and M. Fieux, The Somali Current in autumn 1984, before the onset of the northeast monsoon, *Nature*, *315*, 50–52, 1985.

Schott, F., J. Swallow, and M. Fieux, The Somali Current at the equator: Annual cycle of currents and transports in the upper 1000 m and connection to neighbouring latitudes, *Deep Sea Res.*, *37*, 1825–18481, 1990.

Schott, F., J. Reppin, and J. Fischer, Currents and transports of the monsoon current south of Sri Lanka, *J. Geophys. Res.*, *99*, 25,127–25,141, 1994.

Shankar, D., and S. Shetye, On the dynamics of the Lakshadweep High and Low in the southeastern Arabian Sea, *J. Geophys. Res.*, *102*, 12,551–12,562, 1997.

Shankar, D., J. McCreary, W. Han, and S. Shetye, Dynamics of the East India Coastal Current, 1, Analytic solutions forced by interior Ekman pumping and local alongshore winds, *J. Geophys. Res.*, *101*, 13,975–13,991, 1996.

Shetye, S. R., A. Guveia, S. Shenoi, G. Michael, A. Almeida, and K. Santanam, Hydrography and circulation off the west coast of India during the southwest monsoon 1987, *Deep Sea Res.*, *48*, 359–378, 1990.

Shetye, S. R., S. S. C. Shenoi, G. S. Michael, D. Sundar, A. Almeida, and K. Santanam, The coastal current off western India during the northeast monsoon, *Deep Sea Res.*, *38*, 1517–1529, 1991.

Shetye, S. R., A. Gouveia, S. S. C. Shenoi, D. Sundar, G. Michael, and G. Nampoothiri, The western boundary current of the seasonal subtropical gyre in the Bay of Bengal, *J. Geophys. Res.*, *98*, 945–954, 1993.

Shetye, S., A. Gouveia, D. Shankar, S. Shenoi, P. Vinayachandran, D. Sundar, G. Michael, and G. Nampoothiri, Hydrography and circulation in the western Bay of Bengal during the northeast monsoon, *J. Geophys. Res.*, *101*, 14,011–14,025, 1996.

Simmons, R., M. Luther, J. O'Brien, and D. Legler, Verification of a numerical ocean model of the Arabian Sea, *J. Geophys. Res.*, *93*, 15,437–15,453, 1988.

Smith, L., D. Boudra, and R. Bleck, A wind-driven isopycnic coordinate model of the North and equatorial Atlantic Ocean, 2, The Atlantic basin experiment, *J. Geophys. Res.*, *95*, 13,105–13,128, 1990.

Swallow, J., R. Molinari, J. G. Bruce, O. B. Brown, and R. H. Evans, Development of near-surface flow pattern and water mass distribution in the Somali Basin in response to the southwest monsoon of 1979, *J. Phys. Oceanogr.*, *13*, 1398–1415, 1983.

Toole, J., and B. Warren, A hydrographic section across the subtropical south Indian Ocean, *Deep Sea Res.*, *40*, 1973–2019, 1993.

United Nations Educational, Scientific, and Cultural Organization (UNESCO), *Discharge of Selected Rivers of the World*, vol. 1, 2, and 3, *Stud. Hydrol.*, vol. 5, Paris, France, 1993.

Varkey, M., V. Murty, and A. Suryanarayana, Physical Oceanography of the Bay of Bengal and Andaman Sea, *Oceanography and Marine Biology: An annual Review 1996, 34*, 1–70, 1996.

Vinayachandran, P., Y. Masumoto, T. Mikawa, and T. Yamagata, Intrusion of the southwest monsoon current into the Bay of Benagl, *J. Geophys. Res.*, *104*, 11,077–11,085, 1999a.

Vinayachandran, P., N. Saji, and T. Yamagata, Response of the equatorial Indian Ocean to an unusual wind event during 1994, *Geophys. Res. Lett.*, *26*(11), 1613–1616, 1999b.

Webster, P., A. Moore, J. Loschnigg, and R. Leben, Coupled ocean-atmosphere dynamics in the Indian Ocean during 1997–98, *Nature*, *401*, 359–365, 1999.

Woodberry, K., M. Luther, and J. O'Brien, The wind-driven seasonal circulation in the southern tropical Indian Ocean, *J. Geophys. Res.*, *94*, 17,985–18,002, 1989.

Wyrtki, K., *Oceanographic Atlas of the International Ocean Expedition*, Superintendent of Doc., U.S. Govt. Print. Office, Washington, D. C., 1971.

Wyrtki, K., An equatorial jet in the Indian Ocean, *Science*, *181*, 262–264, 1973.

Yang, J., L. Yu, C. J. Koblinsky, and D. Adamec, Dynamics of the seasonal variations in the Indian Ocean from TOPEX/Poseidon sea surface height and an ocean model, *Geophys. Res. Lett.*, *25*, 1915–1918, 1998.

You, Y., and M. Tomczak, Thermocline circulation and ventilation in the Indian Ocean derived from water mass analysis, *Deep Sea Res.*, *40*, 13–56, 1993.

Yu, L., and M. M. Rienecker, Indian Ocean warming in 1997–1998, *J. Geophys. Res.*, *105*, 16,923–16,939, 2000.

Yu, L., J. O'Brian, and J. Yang, On the remote forcing of the circulation in the Bay of Bengal, *J. Geophys. Res.*, *96*, 20,449–20,454, 1991.

G. Evensen, V. E. J. Haugen, and O. M. Johannessen, Nansen Environmental and Remote Sensing Center, Edvard Griegsvei 3a, 5059 Solheimsviken, Norway. (geir.evensen@nrsc.no; vibeke.haugen@nrsc.no; ola.johannessen@nrsc.no)

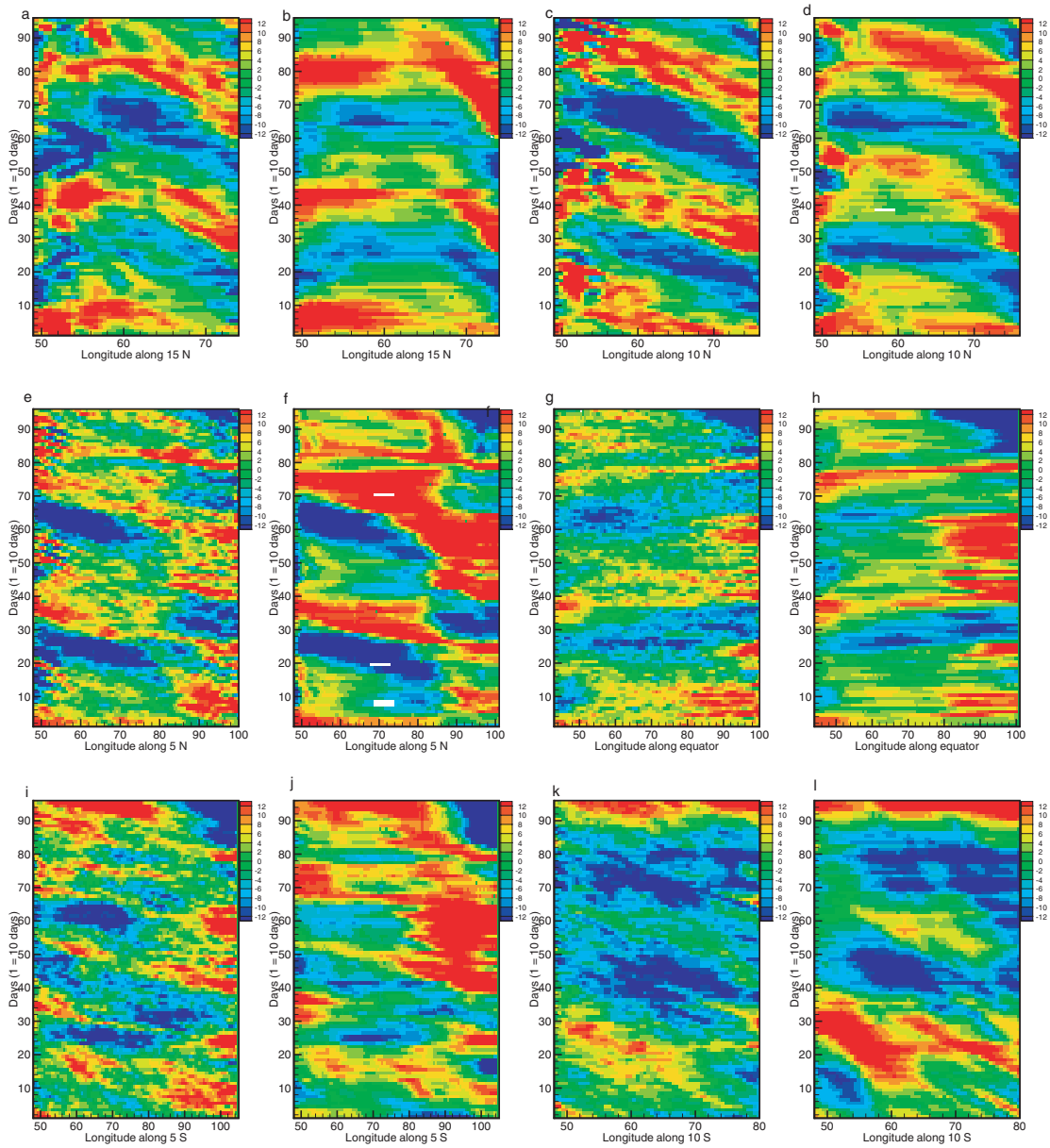

Figure 4. Hovmöller plots from observed (left plot in each pair) and simulated SLA (right plot in each pair) every 5° latitude between 15°N and 10°S from 1995 to 1997 (y axis: 1 = 10 days).

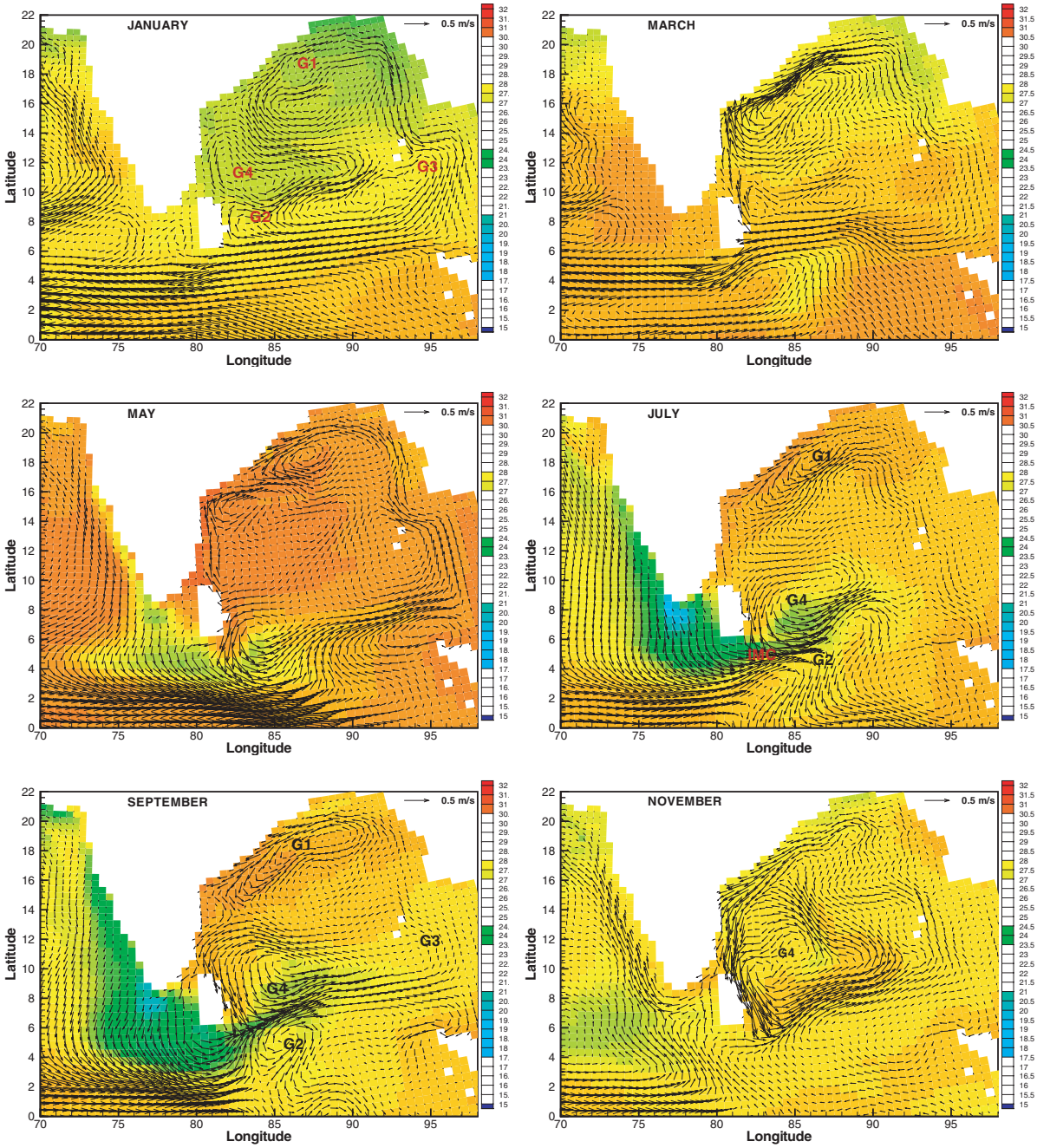

Figure 7. Surface circulation in the Bay of Bengal from the model showing temperature and current velocities for every second month from January to November 1996. G1 to G4 represent the eddies which are discussed in section 4, and IMC is the Indian Monsoon Current.

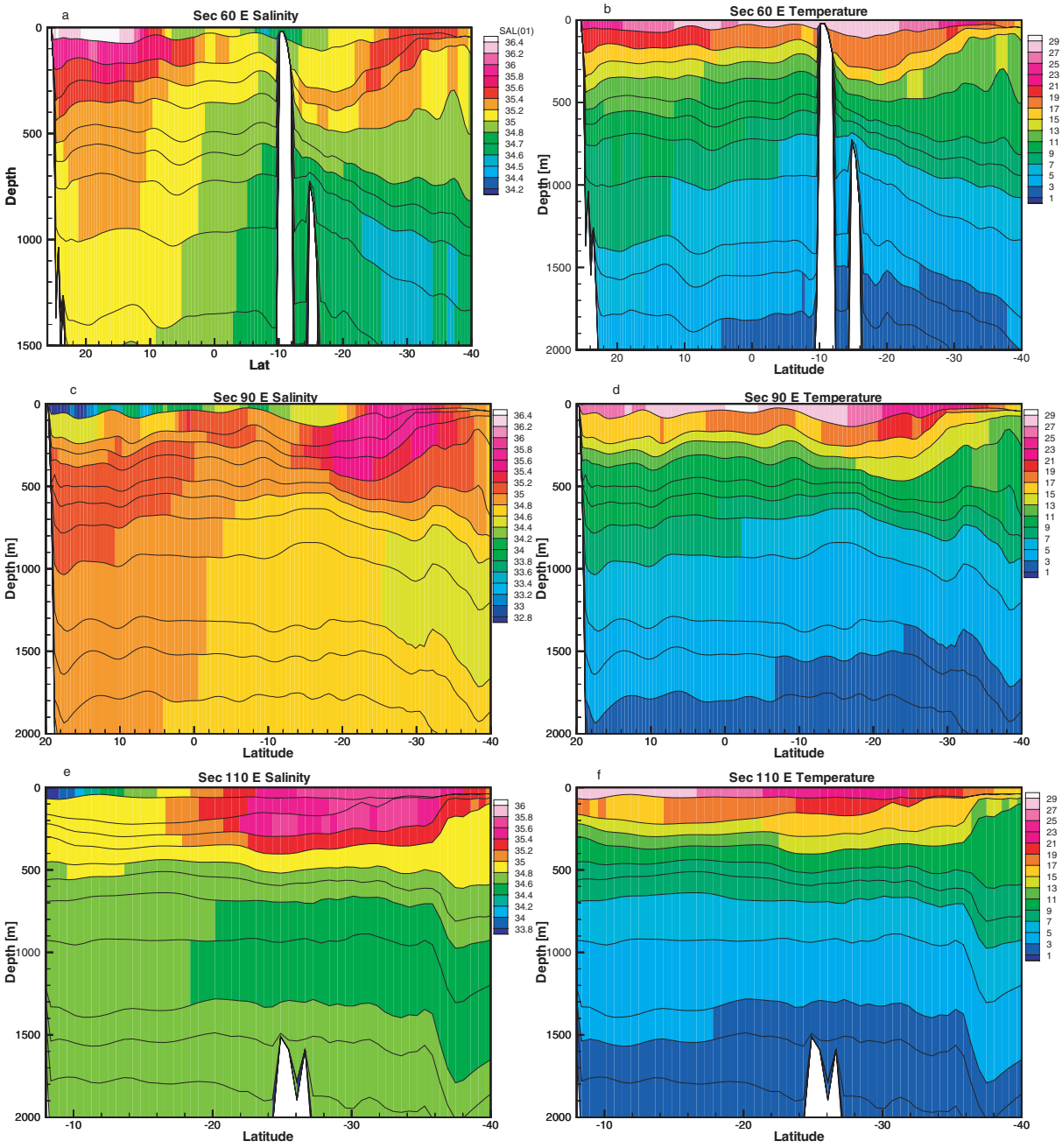

Figure 11. Meridional sections of monthly averaged salinity and temperature in the Indian Ocean during January 1996. The contour levels for the salinity have been chosen to best present the different salinity characteristics along the various sections.

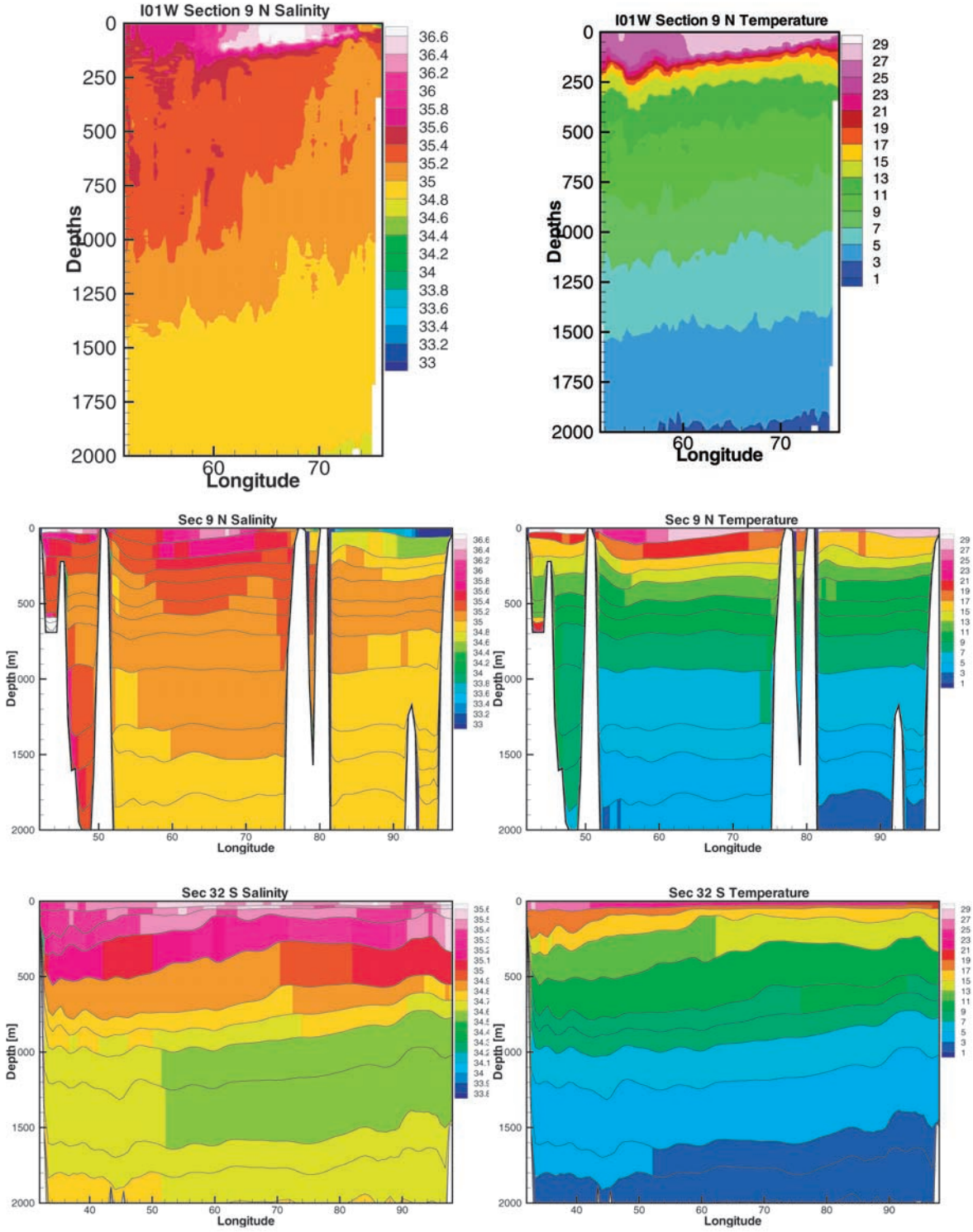

Figure 12. Zonal sections of monthly averaged (left) salinity and (right) temperature in the Indian Ocean. The contour levels for the salinity has been chosen to best present the different salinity characteristics along the various sections. (top) WOCE section along 9°N, (middle) simulated section along 9°N September 1995, (bottom) and simulated section along 32°S January 1996.

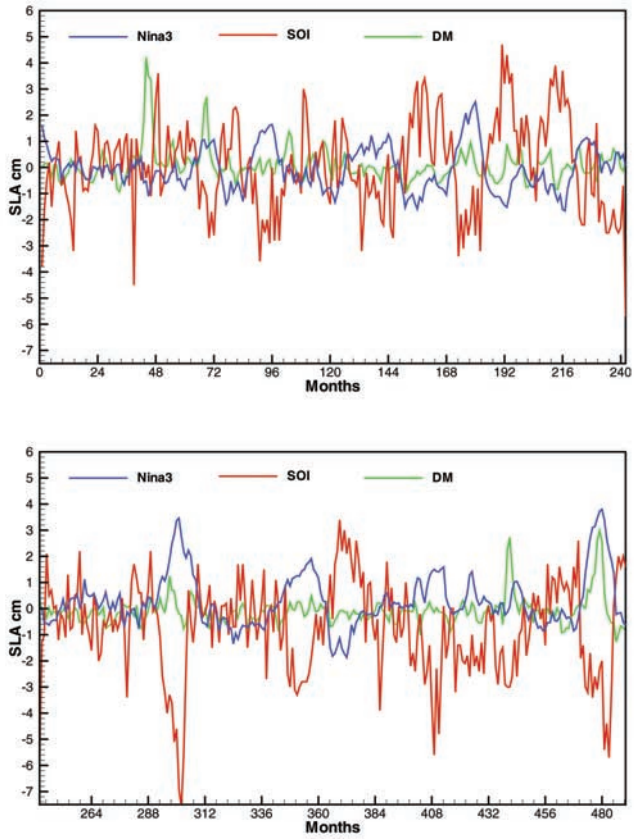

Figure 14. Dipole mode calculated for simulated SSTA, Southern Oscillation Index (SOI), and Nina3 for 1958–1998. SOI gives a measure of the strength and phase of the Southern Oscillation and indicates the status of the Walker circulation. Nina3 represents the El Niño in the Pacific Ocean from SSTA of the central and eastern equatorial Pacific.